

**NOPEX/FOREST-DYNAMO**  
**Ground data collection and data analysis report**

**Fieldcampaigns in 1994-1995**

**P.J. van Oevelen and I.H. Woodhouse**

**RAPPORT 70**

**November 1996**

**Vakgroep Waterhuishouding**  
**Nieuwe Kanaal 11, 6709 PA Wageningen**

**ISSN 0926-230X**

# Contents

<b>1</b>	<b>Introduction</b>	<b>8</b>
1.1	Problem definition and objectives . . . . .	8
1.1.1	Overall scientific objectives and goals of NOPEX . . . . .	9
1.1.2	Objectives and goals of FOREST-DYNAMO . . . . .	10
1.1.3	Anticipated results of FOREST-DYNAMO . . . . .	11
<b>2</b>	<b>Description of experimental sites</b>	<b>12</b>
2.1	General NOPEX area . . . . .	12
2.2	Siggefora . . . . .	12
2.3	Fjärdhundra . . . . .	12
<b>3</b>	<b>Data collection</b>	<b>17</b>
3.1	Biophysical data . . . . .	17
3.2	Soil moisture . . . . .	19
3.2.1	Equipment and calibration . . . . .	19
3.3	Surface roughness and cross section profiles . . . . .	19
3.3.1	Surface roughness measurements . . . . .	19
3.3.2	Cross section profiles . . . . .	21
3.4	Available airborne and spaceborne remotely sensed microwave data	23
3.4.1	Airborne SAR data, EMISAR . . . . .	23
3.4.2	Airborne passive microwave data, EMIRAD . . . . .	23
3.4.3	Spaceborne SAR data . . . . .	23
<b>4</b>	<b>Data analysis and results</b>	<b>25</b>
4.1	Biophysical data . . . . .	25
4.1.1	Tree Growth Model . . . . .	25
4.2	Soil moisture data . . . . .	25
4.3	Surface roughness measurements and cross-section profiles . . . . .	26
4.3.1	Surface roughness measurements . . . . .	26
4.3.2	Cross section profile measurements . . . . .	26
4.4	Remotely sensed data . . . . .	28
4.4.1	EMISAR . . . . .	28
4.4.2	ERS-1 SAR . . . . .	29
4.4.3	ERS-1 WSC . . . . .	30

<b>5 Preliminary results</b>	<b>31</b>
5.1 Modelling with "Treegrow" of Pine and Spruce trees . . . . .	31
5.1.1 Parameterisation of Forest Stands . . . . .	31
5.2 Forward Backscatter Modelling Using the UTA model . . . . .	32
5.2.1 Results . . . . .	32
5.2.2 Summary . . . . .	35
5.3 Inverse modelling of soil moisture . . . . .	35
5.3.1 Theoretical framework . . . . .	35
5.3.2 Results . . . . .	38
5.4 Inversion of Scandinavian WSC Data . . . . .	39
5.4.1 Forward Model . . . . .	39
5.4.2 WSC Inverse Model . . . . .	42
5.4.3 Results . . . . .	43
5.5 Classification and segmentation . . . . .	48
5.5.1 Classification of scattering mechanisms . . . . .	48
5.5.2 Results . . . . .	48
5.5.3 Segmentation . . . . .	49
5.5.4 Results . . . . .	51
5.5.5 Classification of segmented EMISAR data . . . . .	51
<b>A Soil moisture measurements</b>	<b>59</b>
A.1 1994 Soil moisture measurements . . . . .	59
A.2 1995 Soil moisture measurements . . . . .	59
<b>B Forest Floor Cross-Sections</b>	<b>63</b>
<b>C Forest stand parameters</b>	<b>73</b>

# List of Tables

3.1	Table of stand characteristics for 8 stands and 1 clear cut in the Siggefora test area. . . . .	18
4.1	Surface roughness data for the April, 1995 measurements. The numbers refer to the location and are described in Table ?? . . . .	28
4.2	Surface roughness data for the June 1995 measurements. The numbers refer to the location and are described in Table ?? . . . .	28
4.3	Some of the more important characteristics of the EMISAR data available . . . . .	29
4.4	Dates of ERS-1 images that are available . . . . .	30
4.5	Available WSC data of the five regions at the Department of Water Resources. . . . .	30
5.1	An example input file to the backscatter model. The data represent various characteristics of representative cylinders, such as radius, length, angular distribution, etc. . . . .	33
5.2	Comparison of C and L-band observed backscatter with modelled backscatter from Siggefora (observed backscatter from EMISAR July 1995). All values in dB. . . . .	36
5.3	An example of a part of a Look Up Table (LUT) for C-band, HH and VV polarisation. Three different roughness cases, one incidence angle, and a soil moisture range from 0.00 to 0.20 with steps of 0.05 is used to generate this table. . . . .	37
5.4	Surface roughness parameters for the three selected cases used in the INVIEM model for FOREST-DYNAMO. . . . .	37
5.5	TDR volumetric soil moisture content compared with L-band EMISAR estimates using the INVIEM model. Data is taken on June 5, 1995. . . . .	39
5.6	TDR volumetric soil moisture measurements compared with C-band EMISAR estimates. Data is taken on June 6, 1995. . . . .	39
A.1	TDR volumetric soil moisture content measurements performed on June 23, 1994 . . . . .	59
A.2	TDR volumetric soil moisture content measurements performed on May 3, 1995, Tracks A, B and C . . . . .	60
A.3	TDR volumetric soil moisture content measurements performed on May 3, 1995, Tracks D, E and F . . . . .	60
A.4	TDR volumetric soil moisture content measurements performed on July 5 and 6, 1995, Tracks A and B . . . . .	61

A.5	TDR volumetric soil moisture content measurements performed on July 5 and 6, 1995, Tracks C and D . . . . .	61
A.6	TDR volumetric soil moisture content measurements performed on July 5 and 6, 1995, Tracks E and F . . . . .	62
B.2	Cross section height measurements for stand 8B . . . . .	64
B.1	Cross section height measurements for stand 8A . . . . .	65
B.3	Cross section height measurements for stand 17 . . . . .	65
B.4	Cross section height measurements for stand 18A . . . . .	66
B.5	Cross section height measurements for stand 18B . . . . .	67
B.6	Cross section height measurements for stand 20.1 (clear cut) . . .	68
B.7	Cross section height measurements for stand 021 . . . . .	69
B.8	Cross section height measurements for stand 042 . . . . .	70
B.9	Cross section height measurements for stand 044 . . . . .	71
B.10	Cross section height measurements for stand 46.1 . . . . .	72
C.1	Swedish Forestry Service data for the stands in the Siggefora area. Ages are in 1994. . . . .	74

# List of Figures

2.1	Map of the NOPEX region. Dotted lines are flight "legs" co-ordinated with the sites located in forest and bogs (grey), agricultural land (white) and lakes (black). The three dashed areas are EMISAR targets. Notice the location of the test sites near Siggefora(Östfora) and Fjärdhundra. Drawing by Hans Nilsson [?].	13
2.2	More detailed map of the Siggefora site. . . . .	14
2.3	The top of the forest canopy in the Siggefora test site. . . . .	14
2.4	A view into the forest canopy in the Siggefora test site. . . . .	15
2.5	More detailed map of the Fjärdhundra site. . . . .	16
3.1	Visual representation of 3 stages of growth of Scots Pine (15, 20 and 30 year old) using a tree growth model to simulate tree structure. The scale on the left is in metres. . . . .	18
3.2	Soil profile meter or "needle board" . . . . .	20
3.3	Map of the forest stands in the Siggefora test site. . . . .	22
3.4	Geometry of the ERS Windscatterometer instrument. . . . .	24
4.1	Branch statistics for a 67 year old Scots Pine. . . . .	26
4.2	Photograph demonstrating the use of the transparent 1 cm grid-ded pane in a pea field. . . . .	27
4.3	Photograph demonstrating the use of a needleboard to obtain a surface roughness profile. . . . .	27
4.4	Cross section height profiles for some forest stands. . . . .	29
5.1	Representative cross-sections of three of the test stands. From left to right they are, stand 18 (67 year old pine), stand 46.1 (38 year old spruce) and stand 21 (28 year old pine). . . . .	32
5.2	Graphical representation of the stand modelling process. Branches are represented as dielectric cylinders (figure is not to scale). . .	34
5.3	Graphical representation of the Look Up Table generated with the IEM model and the inversion using the INVIEM model. . . .	38
5.4	EMISAR C- and L-band Soil moisture estimates using the INVIEM model compared with TDR measurements for tracks A and B. . . . .	40
5.5	EMISAR C- and L-band Soil moisture estimates using the INVIEM model compared with TDR measurements for tracks C and D. . . . .	40

5.6	EMISAR C- and L-band Soil moisture estimates using the IN- VIEM model compared with TDR measurements for tracks E and F. . . . .	41
5.7	Results of applying the retrieval algorithm to the WSC data over Scandinavia for January and July 1995, showing pairs of percent- age vegetation cover, reflectivity and RMS slope. . . . .	44
5.8	Multi temporal ERS-1 SAR image of the NOPEX test area. The generally colourless areas are coniferous forest. . . . .	45
5.9	The temporal variation of the retrieved percentage vegetation cover and reflectivity for the NopeX test site. The error bars (not shown for reflectivity) indicate the estimated uncertainty on the retrieved values. The horizontal lines indicate the estimated range of vegetation cover from analysis of SAR data of the area. . . . .	46
5.10	Measurements and subsequent modelled response using the re- trieved parameters over the NOPEX test area, for two months in 1995: January and June. The seasonal variation is quite appar- ent between the two data sets, and the retrieved vegetation cover was 38% and 65% for January and June respectively showing good agreement with the expected results. . . . .	47
5.11	C-band scattering classification image of EMISAR data at the Fjärdhubdra site where Red is odd scattering, Green is diffuse scattering and Blue is even scattering. . . . .	49
5.12	L-band scattering classification image of EMISAR data at the Fjärdhubdra site, where Red is odd scattering, Green is diffuse scattering and Blue is even scattering. . . . .	50
5.13	Segmentation result using EMISAR C-band data for the Siggefora test site. . . . .	52
5.14	Segmentation result using EMISAR L-band data for the Siggefora test site. . . . .	53
5.15	A segmentation classification image with the stand borders overlaid. . . . .	54
B.1	Long transect height profile measurements for stands 18 and 44 . . . . .	63

**Remark 1** *This report is an internal report of the Department of Water Resources regarding field work and results within the NOPEX/FOREST-DYNAMO project. None of the contents may be copied (in any form or through any method whatsoever) without the written permission of the authors. This report is solely the responsibility of the authors.*



# Chapter 1

## Introduction

The FOREST Environmental DYNAMics MONitoring and climate research (FOREST-DYNAMO) project is funded through the European Community, under contract EV5V-CT94-0502, to study the potential of airborne and satellite remote sensing for monitoring European boreal environments in support of climate research. The FOREST-DYNAMO project is embedded within the NOthern Hemisphere Climate Processes Land-surface Experiment (NOPEX) as a catalyst for remote sensing research [26]. As such, this project contributes directly to the IGBP Global Change Core Project on Biospheric Aspects of the Hydrological Cycle (BAHC).

In this report a summary and overview is given of the available ground data that was collected during the NOPEX/FOREST-DYNAMO field campaigns held in 1994 and 1995. The first field experiment, referred to as Concentrated Field Effort (CFE), was held from 27 May until 23 June, 1994 (CFE1). The second field experiment (CFE2) was held from 8 May until 16 June, 1995. Before the CFE2 a short field trip was made from April 30 until May 3 to perform fieldwork to support the EMISAR flights and to inspect the field locations for the CFE2. A second trip later that year was made during the second intensive field observation period (28 June until 7 July). More information of these field experiments can be found in the various experimental plans [17][16]. Furthermore, some preliminary results have been added to illustrate the potential of the data available.

### 1.1 Problem definition and objectives

Climatic research has received increasingly more attention over the last few years. Especially the so called "Green House" effect and the resulting climatic change has lead to more awareness of the general public regarding human impact on the climate. Although more research seems to support the idea of the existence of the "Green House" effect the magnitude and resulting effects on local and regional climates are still uncertain.

Since the beginning of the 1980's various large scale field experiments have been executed resulting in large amounts of data for environmental research. Most of these experiments were held in relatively arid and warm areas, e.g. HAPEX-Sahel in Niger [10] and HAPEX-EFEDA in Spain [1]. The reason

being that in these regions the largest extremes in energy and waterbalance can be found and that the environment is most vulnerable to small changes in climatic conditions. However, for global climatic research other regions of the earth must also be investigated to study the impact of climatic changes on a global scale. In North-America the BOREAS experiment and in Europe the NOPEX experiment were initiated to investigate the climate of the more temperate zones, in particular the boreal environments.

### **1.1.1 Overall scientific objectives and goals of NOPEX**

The central objective of the NOPEX project is to study landsurface processes at a regional scale for mixed land cover dominated by boreal forest. This encompasses the transfer of energy, momentum, water and CO<sub>2</sub> between the soil, vegetation and atmosphere on local to regional scales ranging from centimetres to tens of kilometres [17].

This objective will be pursued by:

- Providing improved parameterization schemes of exchange of water, energy and carbon between the land surface and the atmosphere in hydrological and meteorological models from the meso-scale to the global scale;
- Studying the use of satellite and airborne remotely sensed data for evaluation of surface fluxes and states by supplying hard data on the ground truth;
- Quantifying the size of terms in the surface energy balance as well as in the water and carbon balances from different types of landcover, during both daily and annual cycles;
- Explore methods for aggregation and disaggregation of parameters between the three spatial scales; patch scale, intermediate scale and regional scale. Patches may be topographical elements, land use classes, infiltration areas, exfiltration areas etc.;
- Critically evaluate the accuracy needed to measure not only absolute values of surface fluxes but also regional variations in such fluxes;
- Fostering a new community of land-surface experimentalists capable of carrying out experiments in places with bad infrastructure and harsh climate.

The NOPEX project can be subdivided into four thematic groups:

- Local studies: soil physics, biophysics and fluxes;
- Regional scale studies: aeronomy and meso scale. Modelling fluxes;
- Remote sensing: soil physics, biophysics and fluxes;
- Long term studies, including climate and catchment hydrology: soil physics, fluxes, water balance and terrain modelling.

This work and data presented in this report is done within the framework of the thematic group of Remote Sensing. The research in this thematic group is funded through the EC and is referred to as FOREST-DYNAMO.

### 1.1.2 Objectives and goals of FOREST-DYNAMO

For regional and global climate models there is a need for area-average "effective" parameters at a scale running from 10 km for regional-scale models to typically about 100 km for a global climate model (GCM) [11]. Since, it is impossible to obtain these parameters at these scales through traditional field measurements remote sensing is the tool to obtain such information since remote sensing provides spatially integrated measurements. Various types of remote sensing, such as optical, thermal and microwave remote sensing will be used, but the emphasis will be on the use of microwave remote sensing.

The role of remote sensing for climate research is at least twofold: remote sensing as a tool for long-term monitoring of surface properties and natural or anthropogenic changes which may effect the climate system, and for proper parameterisation, implementation and validation of regional and global climate models [11].

Optical and thermal infrared remote sensing will be used primarily for seasonal monitoring land surface properties such as albedo and land surface temperature. Furthermore, these types of remote sensing can be used synergetically with microwave remote sensing to help deal with problems such as scaling and (dis)aggregation, and verification of results.

Microwave remote sensing has the unique feature that it can be used under almost all-weather conditions, since the earth's atmosphere is virtually transparent, even when it rains, at the longer wavelengths. Furthermore, microwave remote sensing, both radar and radiometry, can be used day and night since it does not depend on solar illumination.

The central theme of FOREST-DYNAMO is: *remote sensing for long term monitoring of forest properties*. The project aims at the further development and improvement of all weather monitoring methodologies to determine the surface physical status of boreal forest environments. The following questions are addressed [26]:

- How can backscattering models be used to extract spatially distributed information on the conditions of boreal forest environments?
- How can passive microwave models be used to extract spatially integrated information (low spatial resolution) of the same targets?
- How can polarimetric signatures (active systems) and dual polarization signatures (passive systems) be used to improve information extraction?
- What is the additional value of synergistic (combined active and passive microwave) inversion models?
- How, and to what extent, can these techniques be used to assess the natural and man-induced changes of forest conditions?
- To what extent can radar systems be used to distinguish between 'organised' and 'disorganised' landscapes with respect to the spatial heterogeneity at various scales?

### **1.1.3 Anticipated results of FOREST-DYNAMO**

Because of the twofold role of remote sensing for climate research, the different portions of the spectrum, the different remote sensing technologies and the inherent aspects of temporal and spatial scales, the research activities by the different participants cover a broad spectrum. Therefore the comparison and validation of the results over the NOPEX area forms an essential element of the approach. The final integration of the results is expected to lead to conclusions about the future role of remote sensing in support of climate modelling and for long-term monitoring of surface properties in boreal environments [26].

## Chapter 2

# Description of experimental sites

### 2.1 General NOPEX area

The NOPEX study site lies north west of Uppsala, Sweden, in an area that is dominated by forests of predominately pine and spruce (approx. 15% are deciduous trees). The site was chosen mainly for its flatness (about 30-70 m asl, with extremes at 1 and 131m asl) and the presence of large patches of mixed boreal-forest and agricultural areas. Furthermore, the distance to the sea is approximately 50 km, avoiding complications of land-seas circulation. The site is on the southern limit of the boreal forest zone with a climate that is more maritime than is usual for boreal forest. The geology of the region is characteristically Northern European: granite, sedimentary gneiss and leptite. The main measurement sites for this study are located in the forest at Siggefora, Östfora, about 30 km Northwest of Uppsala, and the agricultural area around Tisby near Fjärdhundra, about 35 km West of Uppsala (Fig. 2.1).

### 2.2 Siggefora

The Siggefora site (Figure 2.2) is dominated by Norwegian Spruce (*Picea abies*) and Scots Pine (*Pinus sylvestris*). Height differences throughout the forest are small with a total change of elevation of less than 15 m over the 4 km<sup>2</sup> area of the Siggefora test site. Individual stands were chosen for ground truth measurements on the basis of species homogeneity and spatial uniformity.

In Figures 2.3 and 2.4 the top of the canopy of the forested area of Siggefora is shown. Pictures are taken from the meteorological tower, marked by a cross in Figure 2.2, at a height of approximately 20m.

### 2.3 Fjärdhundra

The agricultural area around Tisby near Fjärdhundra is characterised by gentle slopes. The soil types are predominantly clay and clay-loams. The dominant crops are wheat and barley, other crops like peas and rapeseed can also be found.

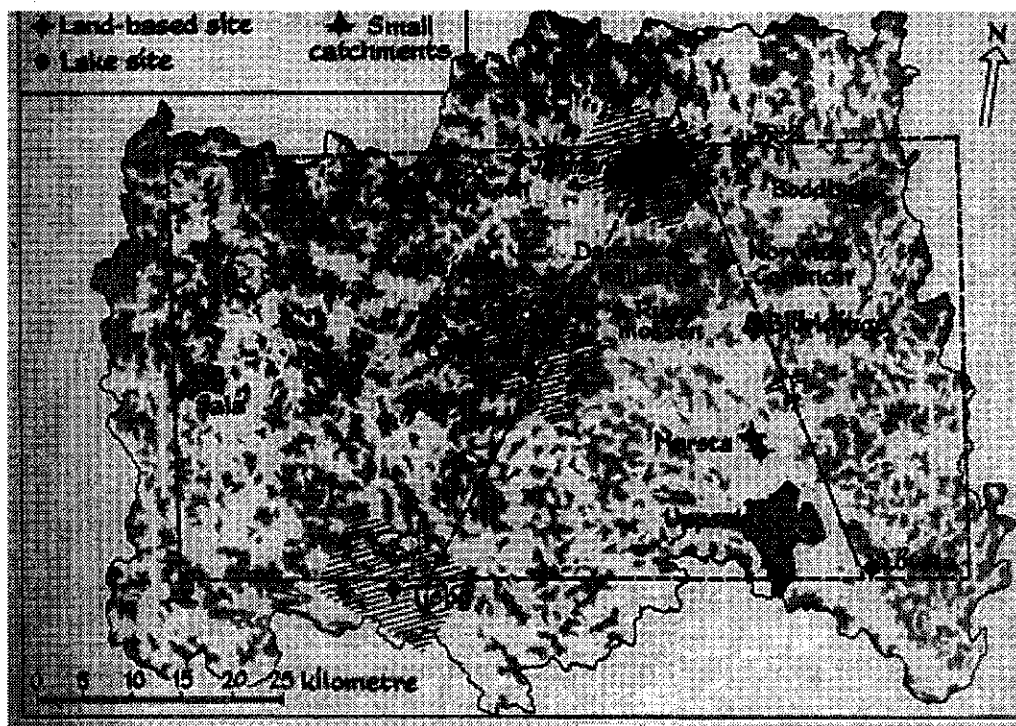


Figure 2.1: Map of the NOPEX region. Dotted lines are flight "legs" coordinated with the sites located in forest and bogs (grey), agricultural land (white) and lakes (black). The three dashed areas are EMISAR targets. Notice the location of the test sites near Siggefora(Östfora) and Fjärdhundra. Drawing by Hans Nilsson [?].



Figure 2.2: More detailed map of the Siggefora site.



Figure 2.3: The top of the forest canopy in the Siggefora test site.

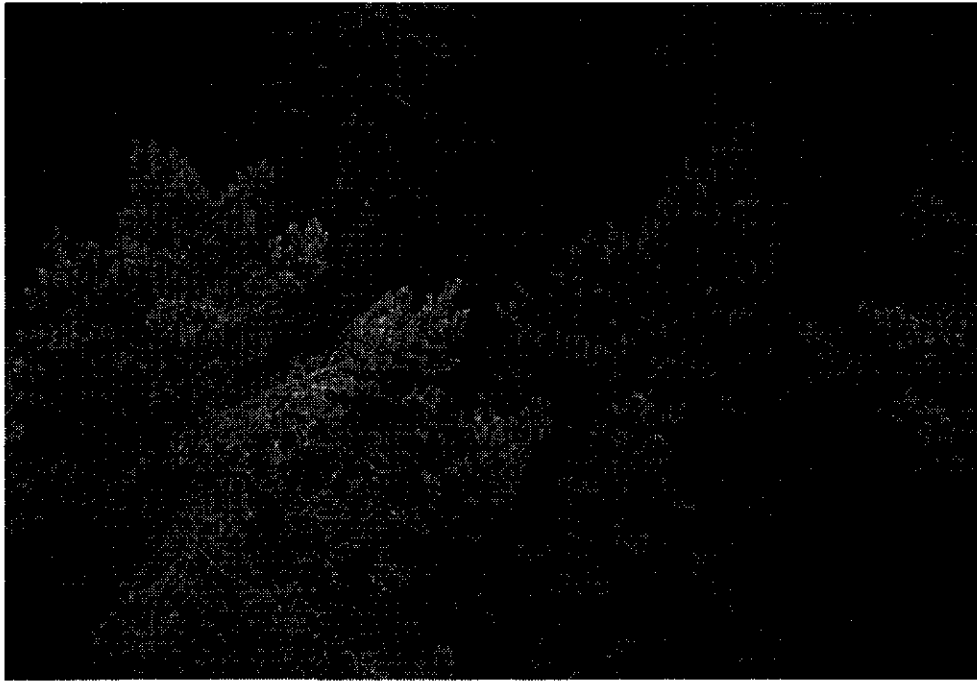


Figure 2.4: A view into the forest canopy in the Siggefora test site.

In Figure 2.5 a detailed map is given showing the location and measurement transects.



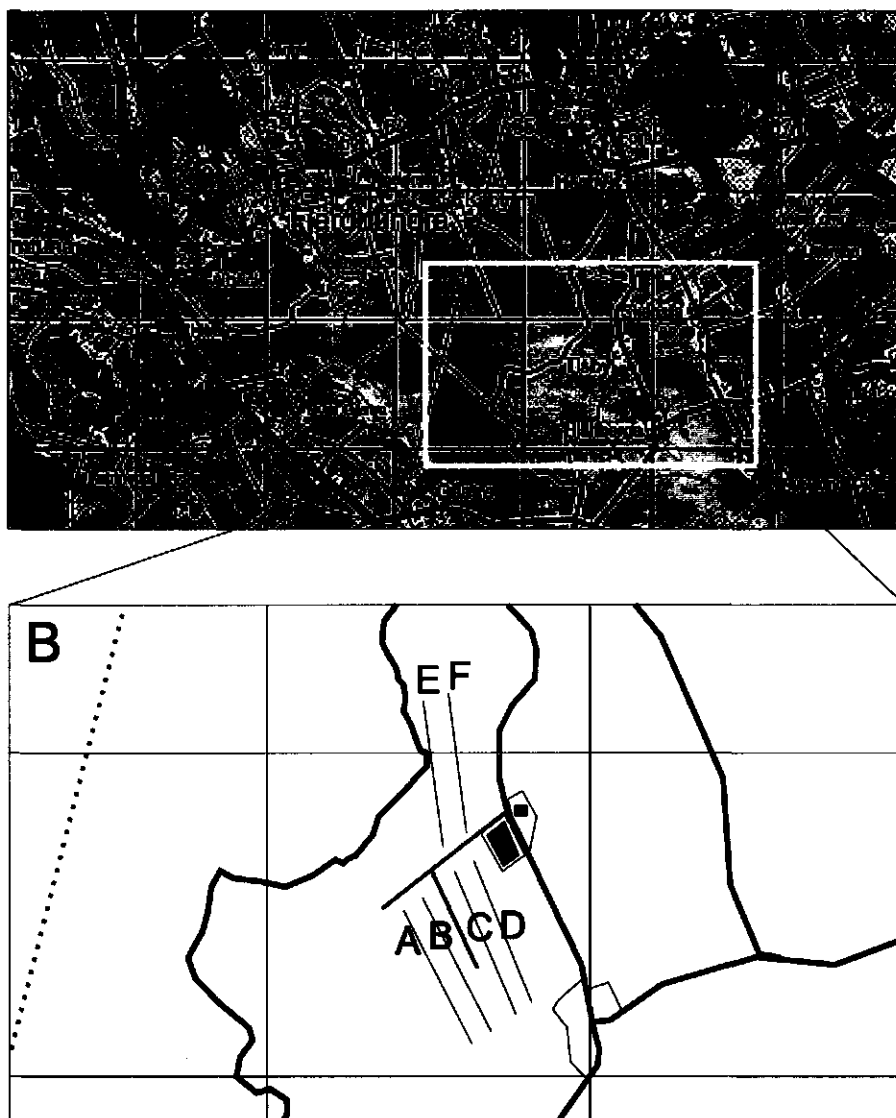


Figure 2.5: More detailed map of the Fjärdhundra site.

## Chapter 3

# Data collection

In 1994 the ground data collection focussed on obtaining input data for the TreeGrow model and input for the SAR soil moisture retrieval algorithm. In 1995 the emphasis was put on collecting additional data for the TreeGrow model [15] and to verify the model results obtained so far. Furthermore, more data was also collected for the SAR soil moisture retrieval algorithm.

### 3.1 Biophysical data

During 1994 ground data collection of forest parameters involved destructive sampling of six representative trees of three different ages and species (ie, 3 each of Norwegian Spruce and Scots Pine). Measurements of age, shoots, number of branches and details of physical dimensions (ie, diameter, length, angle of inclination) of each tree component were made in order to parameterise the tree growth model (described in Sections 4.1, 5.1). The growth model can then be used to simulate trees of varying ages that are typical of those found in the Siggefora test site. An example of three simulated trees is shown in Figure 3.1 which illustrates different stages of growth of a Scots Pine. From such simulations, statistical distributions of branch characteristics may be estimated and used as input to the backscatter model. The value of such a method is the ability to simulate the characteristics of tree stands without the need for further intensive field measurements.

During the two CFE's in 1995 measurements of stand parameters were made: these included tree (species) density, diameter at breast height (dbh), visual estimates of canopy height and depth for 8 stands. The accumulated data, including information gained from the Swedish Forestry Service, are shown in Table 3.1. The stand locations can be found in Figure 5.1. In appendix C a more complete overview is given of stand parameters collected by the Swedish Forestry Service.

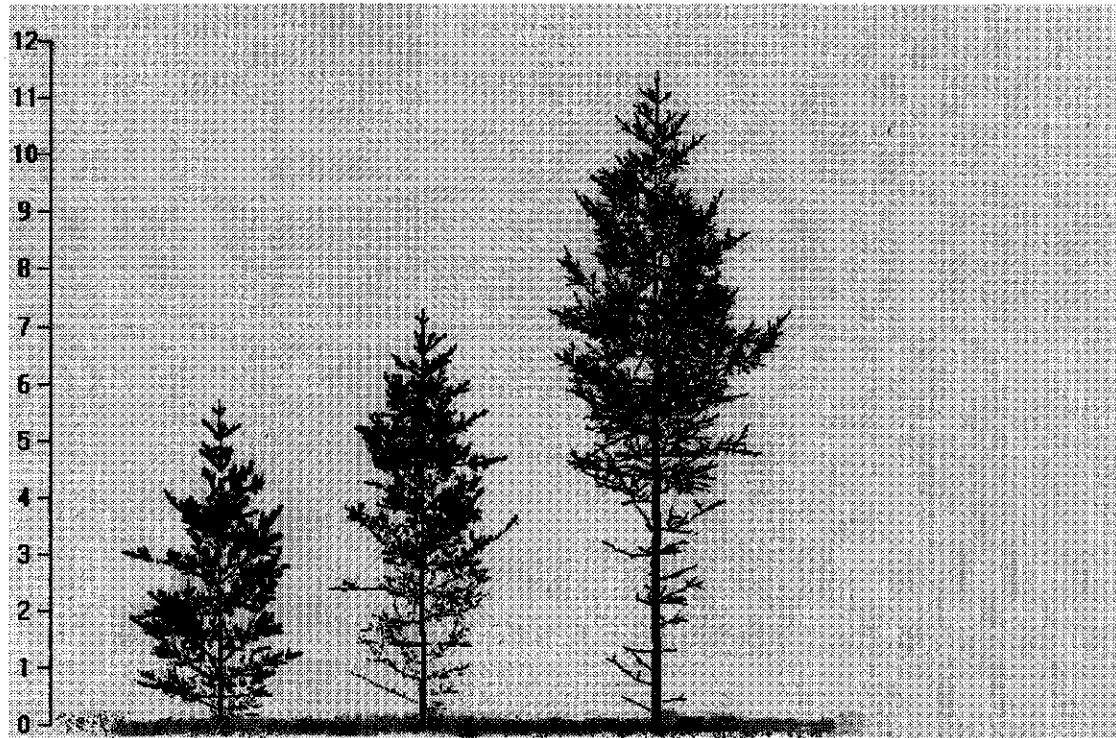


Figure 3.1: Visual representation of 3 stages of growth of Scots Pine (15, 20 and 30 year old) using a tree growth model to simulate tree structure. The scale on the left is in metres.

Swedish Forestry Service Data					WAU data						
Stand No.	Stand area (ha)	Age (est.)	Pine %	Spruce %	no. pines per 15m <sup>2</sup>	no. spruce per 15m <sup>2</sup>	Pine %	Spruce %	Estimated mean height (m)	Average area/ tree (m)	volume/m <sup>2</sup> (m)
008a	13.2	104	90	10	4	13	24	76	20	13.2353	238.7
008b	13.2	104	90	10	8	2	80	20	20	22.5	140.4
017	7.3	91	40	60	3	9	25	75	18	18.75	168.5
018a	3.3	66	100	0	18	0	100	0	8	12.5	151.1
018b	3.3	66	100	0	15	0	100	0	8	15.0	125.9
20.1	1.5	4	80	20	0	0	0	0	0		
021	11.9	27	100	0	61	0	98	0	8	3.68852	40.4
042	3.4	28	100	0	19	0	100	0		11.8421	13.8
044	7.4	66	70	30	11	1	92	8	15	18.75	88.9
046.1	5.4	37	0	100	0	32	0	100	7	7.03125	51.4
047	5.2	70	30	60	14	17	45	55		7.25806	196.1

Table 3.1: Table of stand characteristics for 8 stands and 1 clear cut in the Siggefora test area.

## 3.2 Soil moisture

### 3.2.1 Equipment and calibration

The soil moisture data is collected over a depth of about 6 cm using a Time Domain Reflectometry (TDR) system [24]. The system used was the TRIME P2 system consisting of a probe with two parallel rods of 12 cm length connected with a coax cable to the main module which has a digital display giving the volumetric soil moisture content. The rods of the probe are fully inserted into the ground under an angle of about 30° with the surface resulting in a measurement of the average volumetric soil moisture content over a depth of approximately 6 cm. During the 1995 campaigns the rod was also inserted at an even larger angle to obtain measurements over an depth of approximately 3cm. For a detailed discussion about TDR the reader is referred to Heimovaara and Bouten (1990) and Dasberg and Dalton (1985).

## 3.3 Surface roughness and cross section profiles

### 3.3.1 Surface roughness measurements

The soil surface roughness, an important quantity in microwave remote sensing modelling, is determined using a needle board (see Fig 3.2). The needle board consists of two aligned areas with different density of needles by which the measurements can be made. Macro roughness can be measured with low density sampling (1 needle per cm) and micro roughness can be measured with high density sampling (3 needles per cm). Each measurement gives 151 samples in both high and low density, where the high density is measured over 50 cm and the low density over 150 cm [29]. The needle board has to be placed level over the surface, the needles can then be lowered such that the top of the needles just hit the surface and altogether give a profile of the soil surface. Of the whole board a photograph is taken and the profile can then be digitised. In this way two sets of  $x, z$  coordinates is given for each pair of needles, where "x" stands for the distance between the needles and "z" is the height of the needles.

The number of measurements made is limited to those surfaces that were distinct and representative for the area. For each measurement location two pairs of measurements are made, resulting in one perpendicular to the row direction (the "y" direction) and one parallel to it (the "x" direction). Since we assume that the physical processes that cause surface roughness are uncorrelated for both directions, measurements restricted to these two directions are sufficient.

There are several ways to express the surface roughness. In this report we take the root mean square (RMS) (mm) of the height differences,  $\sigma$ , of the needles, and the autocorrelationlength (cm),  $l$ , as a measure of surface roughness. With these values the power density spectrum using the fast fourier Transform (FFT), and the Autocorrelation function using an inverse FFT can be calculated using the algorithms from Press et al. (1992).

Estimations of root mean square height or  $\sigma$  can be determined directly from samples of  $h(x)$  and  $h(y)$ , yielding  $\sigma_y$  and  $\sigma_x$ . Likewise estimations of the autocorrelation functions  $C(x)$  and  $C(y)$ , in x- and y-directions respectively, follow. Because of the assumed independence between the two directions,

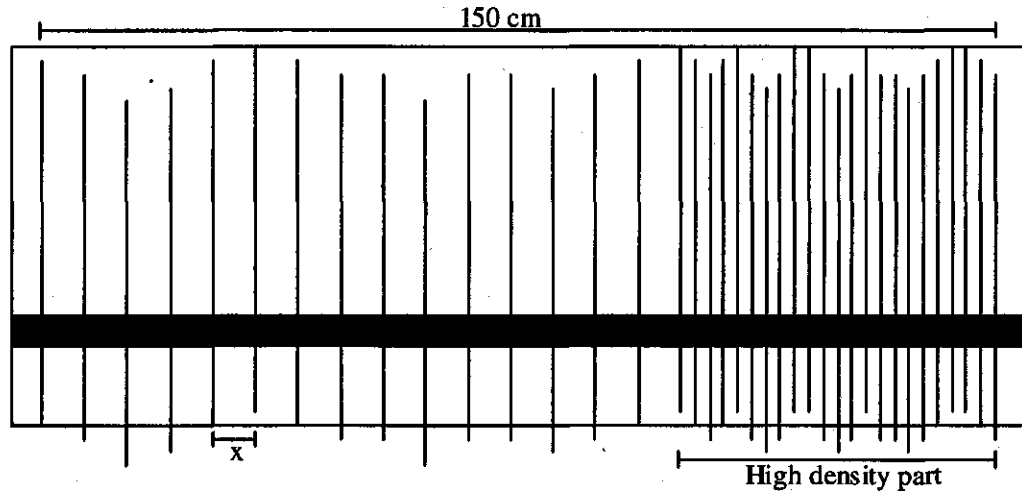


Figure 3.2: Soil profile meter or "needle board"

$C(r) = C(x)C(y)$ . The autocorrelation lengths  $l_x$  and  $l_y$  are defined as the distance at which the normalised autocorrelation functions (for which  $C(0) = 1$ ) fall off to a value of  $1/e$ .

The power spectral density function (or power spectrum) is usually defined as the Fourier transform of the unnormalised autocorrelation function:

$$W(\bar{k}) = \frac{\sigma^2}{(2\pi)^2} \int_{-\infty}^{\infty} C(r) \exp(i\bar{k}r) dr$$

and is also called the surface roughness spectrum. Here  $\bar{k}$  is the spatial wave number of the surface ( $k = 2\pi/\lambda$ ), which in this case is related to the electromagnetic wave number  $k$  by the expression:

$$\bar{k} = 2k \sin \theta_i$$

Also from the power spectral density (PSD) function the autocorrelation lengths  $l_x$  and  $l_y$  can be derived from the points where the normalised PSD function falls off to the value  $1/e$  as  $l_{x,y} = \frac{2}{k_{x,y}}$ . Using the theorems of Wiener-Khintchine and Parseval [22] it can easily be shown that the total area under the power spectrum gives the variance, or 'power' of the surface:

$$\int_{-\infty}^{\infty} W(\bar{k}) d\bar{k} = \sigma^2$$

The theory of wave scattering from rough surfaces often assumes that surface autocorrelation functions are Gaussian and may be given as:

$$C(r) = \exp\left(\frac{-r^2}{l^2}\right)$$

Then, the surface roughness spectrum  $W(\bar{k})$  follows as:

$$W(\bar{k}) = \frac{\sigma^2 l^2}{4\pi} \exp\left(-\frac{\bar{k}^2 l^2}{4}\right)$$

or in the direction of the wave:

$$W(2k \sin \theta_i, 0) = \frac{\sigma^2 l^2}{4\pi} \exp\left(-\bar{k}^2 l^2 \sin^2 \theta_i\right)$$

The power spectral density describes both the spread of heights about the mean plane and the height variation along the surface.

Alternative forms of the correlation function can also be given. The exponential form seems to fit measured surface roughness data better. The exponential correlation function can be written as:

$$C(r) = \exp\left(-\frac{|r|}{l}\right)$$

For higher order surface properties, such as surface gradients, this function poses problems because of the discontinuity at the origin. The surface spectrum for the exponential function becomes:

$$W(\bar{k}) = \frac{\sigma^2}{l^2 \pi^2} \frac{1}{\left(\frac{1}{l^2} + \bar{k}^2\right)}$$

Various other correlation function have been suggested. Furthermore it should be noted that surfaces may be described by more than one correlation function. This can be the case, for instance, for surface whith roughness caused by different types of processes. More detailed information on surface roughness descriptions can be found in Ogilvy (1990).

### 3.3.2 Cross section profiles

In forested areas the surface roughness is difficult to measure. Large amount of debris such as dead branches and leaves hamper accurate measurements. Instead of looking at the micro-roughness, the large surface height variation, resulting from rock outcrops for instance, is considered. The height profile was determined qualitatively for some transects at the Siggefora forest site. The attempts in April 1995 to provide more quantitative measurements were hampered by unseasonal snow cover. However, since the current study has concentrated on stands with dense forest cover the effect of inaccurate surface parameters is considered to be negligible at the frequency considered. However, in June 1995 some more accurate height profiles have been obtained. These were made using a surveying level for seven of the eight test stands (stand 47 was not considered), with perpendicular height transects being made of the forest floor at 10 cm intervals over a distance of 10 m. Two height transects were also made for a clear cut (stand 20.1). Additionally, two 30 m transects were made in stands 18 and 44 (Figure 5.1).

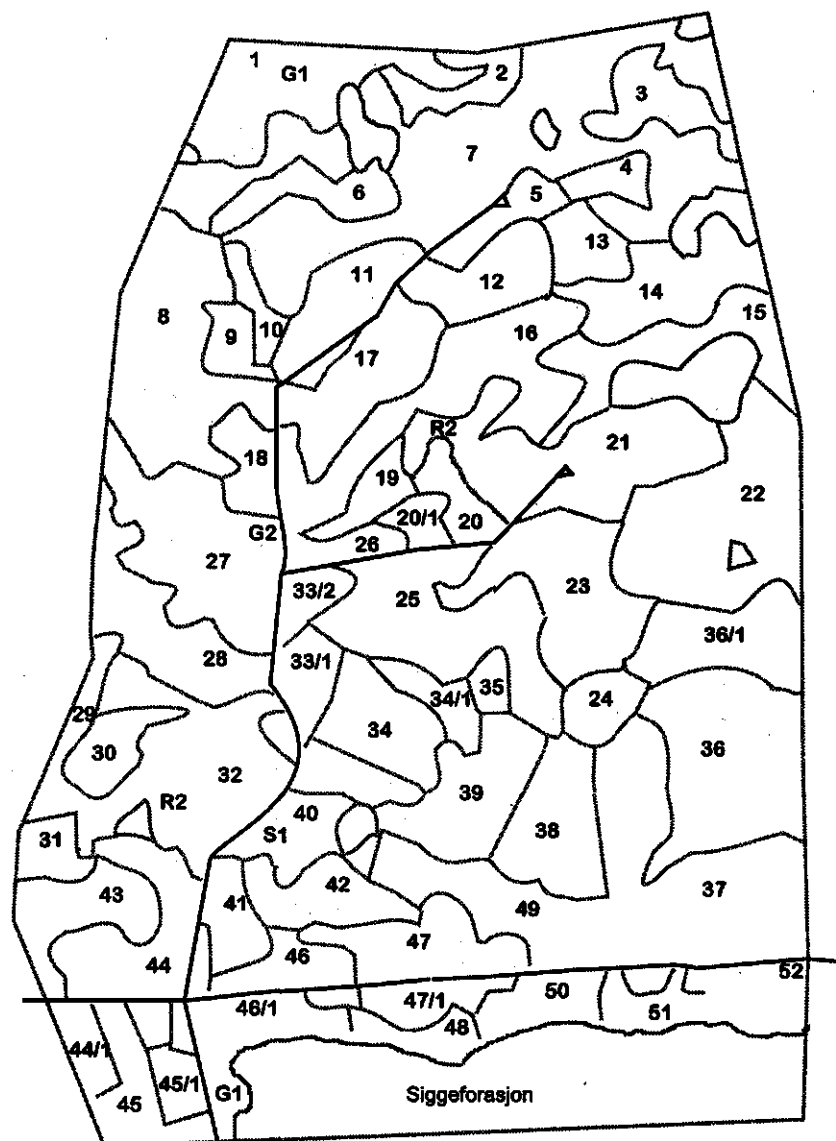


Figure 3.3: Map of the forest stands in the Siggefora test site.

### **3.4 Available airborne and spaceborne remotely sensed microwave data**

#### **3.4.1 Airborne SAR data, EMISAR**

Multipolarisation, C-band (5.3 GHz) SAR data of the Siggefora region were acquired on 23 June 1994 with the airborne SAR system of the Danish Center for Remote Sensing (EMISAR) flown on a Gulfstream G-3 aircraft of the Royal Danish Air Force [3]. The flight of the EMISAR instrument covered a triangular flight line with an image centre incidence angle of 50 and a ground resolution of 2.0-m in both range and azimuth. An additional L-band option with full polarimetric capability has been implemented during the 1995 NOPEX field campaign.

The EMISAR instrument was flown in 1994 on June 23 (C-band, 3 scenes) and in 1995 employed on May 1 (L-band, 4 scenes), May 3 (C-band, 2 scenes), July 5 (L-band, 2 scenes) and July 6 (C-band, 2 scenes). The scenes always included Fjårdhundra and Siggefora.

#### **3.4.2 Airborne passive microwave data, EMIRAD**

The EMIRAD instrument has not been operating as was anticipated. The 1.5 GHz data could not be used due to interference. The 5 GHz data could not be used for quantitative analysis since a smoothing algorithm was applied by the TU-Denmark. Only the 17 and 34 GHz data was usable. Since the research group at the Department of Water Resources, WAU would mainly be interested in the 1.5 and 5 GHz data sets the EMIRAD data will not be used for further analysis in this report.

#### **3.4.3 Spaceborne SAR data**

##### **ERS-1 SAR**

The ERS-1 SAR is a single frequency and polarization radar operating at C-band (5 GHz) and VV-polarization. The spatial resolution of the instrument is approximately 25m and the data are delivered with a pixel size of 12.5m. The look angle of the instrument at the center of the swath is 23°.

##### **ERS-1 WSC**

The ERS-1 Wind scatterometer (WSC) was designed to obtain information on wind speed and direction over the sea surface. It operates by measuring the variation in the radar reflectivity of the sea as a function of look angle due to the presence of small ripples made by the wind close to the water surface. The instrument consists of 3 antennas producing 3 beams looking 45° forward, sideways and 45° backwards with respect to the satellite's flight direction (see Figure 3.4). These beams continuously illuminate a 500 km wide swath as the satellite moves along its orbit. Across the swath local incidence angles range from 18-47° for the midbeam and 25-59° for the forward and aft beams, and 19 measurements are made across the swath. Thus three backscatter measurements at each grid point are obtained at different viewing angles and separated by a short time delay. These triplets are then used routinely to extract wind



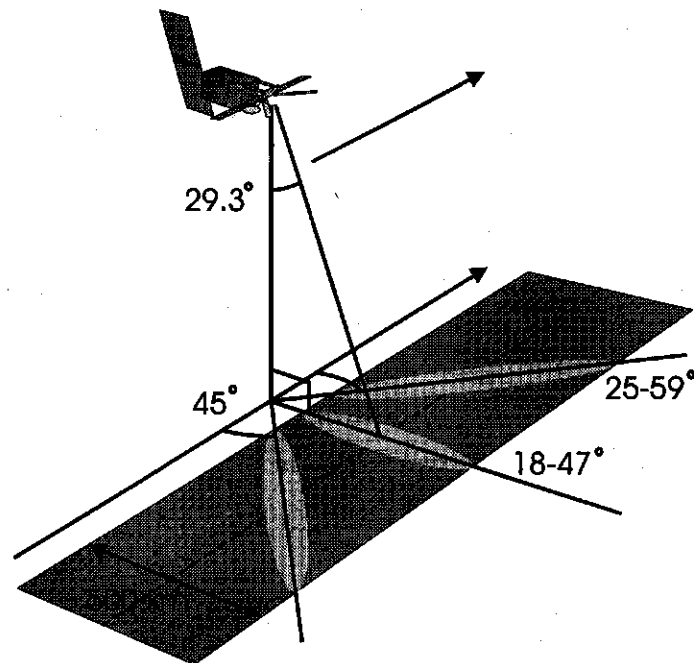


Figure 3.4: Geometry of the ERS Windscatterometer instrument.

speed and direction over sea surfaces through the use of mathematical models. Measurements are also made over land surfaces and these triplets can therefore be used to retrieve surface parameters over land.

The Wind Scatterometer has a spatial resolution of the order of 45 km along and across track with a radiometric stability of  $<0.57$  dB, and a localisation accuracy of better than 5 km. The operating frequency is 5.3 GHz with vertical transmit and receive (VV) polarisation.

The Wind Scatterometer is mounted on the ESA ERS-1 platform. The satellite has a near circular, polar, sun synchronous orbit with an inclination of 98.52 degrees and altitude of 782 to 785 km. The ERS-SAR and the wind Scatterometer cannot operate simultaneously.

## **Chapter 4**

# **Data analysis and results**

### **4.1 Biophysical data**

#### **4.1.1 Tree Growth Model**

The tree growth model uses species dependent branching statistics coupled with other local variables such as lighting conditions, maximum tree height, etc., to simulate the physical structure of trees of a given age, with branches represented by collections of cylinders [15]. From such simulations, statistical distributions of branch characteristics may be determined and used as input to the backscatter model.

The model was parameterised using the destructive structural measurements described in Section 3.1 and then used to simulate trees typical of those found in the Siggefora test site. A visual representation of some simulated trees is shown in Figure 3.1, illustrating different ages of a Scots Pine.

The model can produce a variety of statistical information about branch dimensions, ages, locations and angular distributions, which can be grouped together in terms of any parameter, such as cylinder dimensions or branch order. An example of the distributions obtained from a simulated 67 year old Scots Pine is shown in Figure 4.1. The data from the tree growth model is therefore readily adapted for use as input to the backscatter model.

### **4.2 Soil moisture data**

Soil moisture measurements are available for 1 day (June 23) in 1994 during the CFE1, and 3 days (May 3 and July 5, 6) in 1995 during the CFE2. Snow cover prevented soil moisture measurements on May 1, 1995.

Soil moisture measurements are available for usually 6 transects covering various fields. The original data is given in Appendix B.

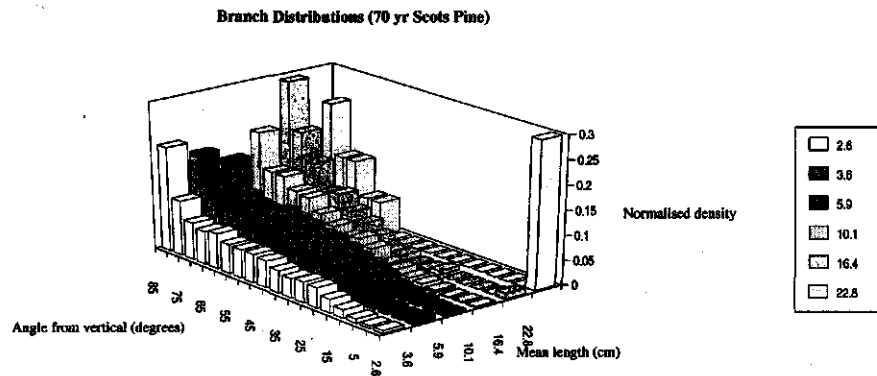


Figure 4.1: Branch statistics for a 67 year old Scots Pine.

### 4.3 Surface roughness measurements and cross-section profiles

#### 4.3.1 Surface roughness measurements

During the 1994 campaign (CFE1) only qualitative soil roughness data are available in the form of photographs showing a transparent pane with 1 cm grid (see Figure 4.2). These data are difficult to interpret and therefore not used in the quantitative analysis (c.f. needleboard in Figure 4.3). They do indicate that the surface roughness appears to be comparable to the situation in the summer of 1995. Actually, the pictures of the transparent gridded pane could be very well used for interpretation of vegetation height characteristics.

For 1995 two sets of roughness measurements are available. The first set is measured in April of 1995 over bare soils under saturated conditions (Table 4.1). The second set is measured during July of 1995 when the crops were present (Table 4.2).

#### 4.3.2 Cross section profile measurements

Examples of cross section profiles of some transects are shown in Figure 4.4, indicating the irregularity of the forest floor. Of the stands measured, the one exception was stand 46.1. This is a dense spruce stand, where the trees have been planted in regular rows: the perpendicular transects for this stand were made so that they were parallel and perpendicular to the row direction.

Tables of the full set of measurements are given in Appendix B.

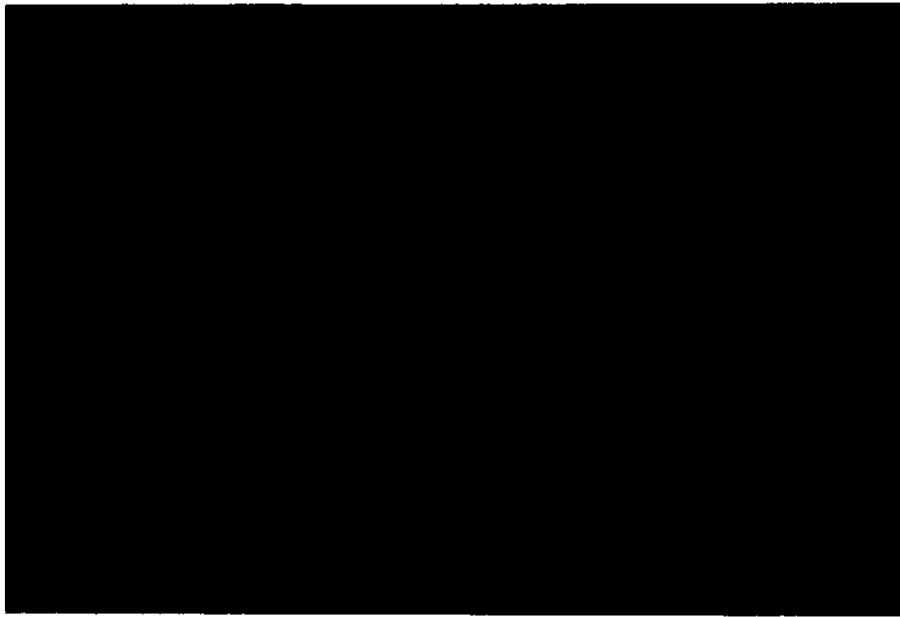


Figure 4.2: Photograph demonstrating the use of the transparent 1 cm gridded pane in a pea field.

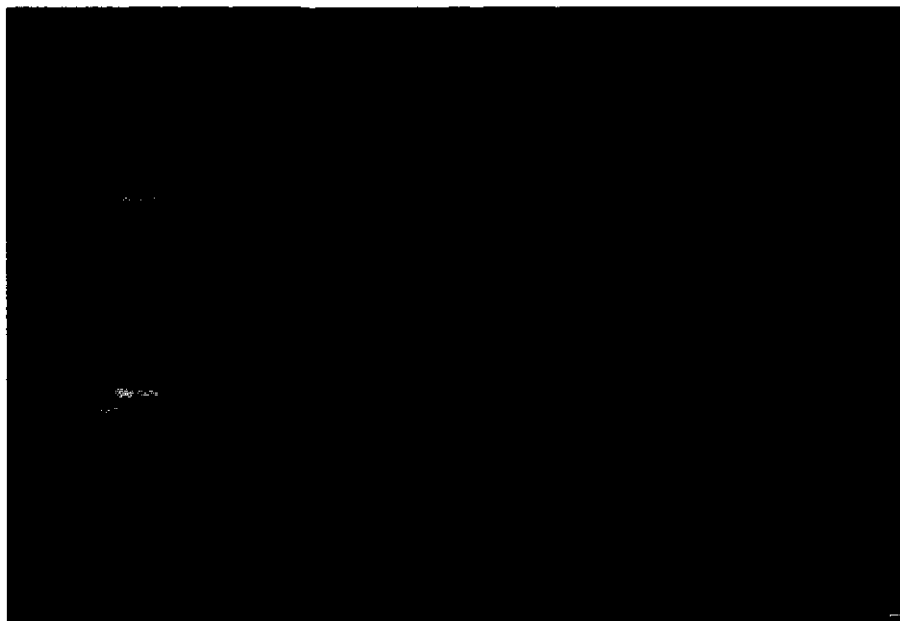


Figure 4.3: Photograph demonstrating the use of a needleboard to obtain a surface roughness profile.

#	Slope [-]	$\sigma_{uncor}$ [mm]	$\sigma_{cor}$ [mm]	$l_{exp.}$ [cm]	$l_{Gaussian}$ [cm]
1	-0.0402014	15.8764	15.5949	14.4931	16.8811
2	0.0261485	26.3429	26.2716	13.9301	16.0743
3	0.0377664	26.7692	26.6227	14.9282	16.8595
4	0.0882091	17.3780	16.1039	17.2897	20.8329
5	-0.0852646	27.1016	26.3560	11.3076	12.9208
6	-0.1704777	21.5509	17.4672	9.24651	-
7	-0.0509065	11.1582	10.5023	6.57298	7.53122
8	-0.0043845	6.49966	6.49154	5.43765	-
9	0.0700566	11.2073	9.93415	4.36390	5.41132
10	-0.0648753	8.94319	7.54356	2.31321	1.71303
11	-0.0237138	31.3960	31.3468	13.3034	16.1142
12	-0.0817147	17.3832	16.2962	14.8373	17.8325
13	-0.0773413	21.6041	20.8313	16.8266	19.4734
14	-0.0716952	14.9215	13.9453	12.3246	15.2340

Table 4.1: Surface roughness data for the April, 1995 measurements. The numbers refer to the location and are described in Table ??

#	Slope [-]	$\sigma_{uncor}$ [mm]	$\sigma_{cor}$ [mm]	$l_{exp.}$ [cm]	$l_{Gaussian}$ [cm]
1	0.0456530	35.3098	35.1476	-45.7385	-
2	-0.0285678	16.0481	15.9081	1.35443	-
3	-0.0536696	29.0454	28.7722	1.68244	2.01082
4	0.0641569	23.1963	22.7046	6.32779	-
5	-0.181366	18.0265	12.0254	5.40011	5.93728
6	0.0276190	11.2222	11.0343	1.28038	-

Table 4.2: Surface roughness data for the June 1995 measurements. The numbers refer to the location and are described in Table ??

## 4.4 Remotely sensed data

### 4.4.1 EMISAR

In 1994 only one dataset came available, namely a C-band ( $f = 5.3$  GHz) full polarimetric data set acquired on June 23. The original complex data with a spatial resolution of  $1.5 \times 1.5$ m have been ground range projected to  $1.5 \times 1.5$ m resolution in ground grid, amplitude detected and lowpass filtered and spatially resampled to  $4.5 \times 4.5$ m. The cross-pol. dataset is the sum of the HV and VH dataset. The look angle range is from  $35.9^\circ$  near range,  $52.0^\circ$  mid range to  $60.2^\circ$  far range. The image is in gamma (linear). For the ground range projection an altitude of 12391m above a flat earth is assumed.

In 1995 two datasets came available, namely a C-band full polarimetric data set acquired on July 6 and a L-band ( $f = 1.25$  GHz) full polarimetric data set acquired on July 5. The original complex scattering matrix data with a spatial resolution of  $1.499 \times 1.500$ m have been converted to covariance matrix data in ground range lowpass filtered and spatial resampled to  $5 \times 5$ m. The cross-pol. dataset is the coherent sum of the HV and VH dataset and divided by two.

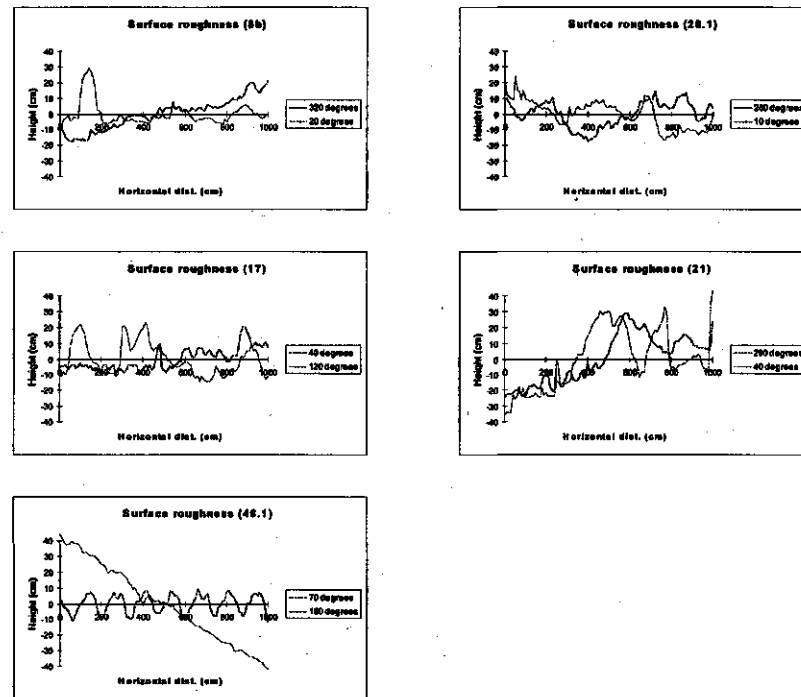


Figure 4.4: Cross section height profiles for some forest stands.

The look angle range is from 33.9° near range, 51.0° mid range to 59.6° far range. The image is in sigma nought (linear). For the ground range projection an altitude of 12387m above a flat earth is assumed. In Table 4.3 the most important characteristics of the data are summarised.

Date	Frequency [GHz]	Resolution [m]	Polarisations	Look angle range	Radiometric values
23-06-1994	5.3	4.5	all	35.9 - 60.2	gamma
05-07-1995	1.25	5.0	all	33.9 - 59.6	sigma
06-07-1995	5.3	5.0	all	33.9 - 59.6	sigma

Table 4.3: Some of the more important characteristics of the EMISAR data available

#### 4.4.2 ERS-1 SAR

The dates of the available ERS-1 instrument data are summarised in Table 4.4.

The ERS-1 SAR data is only preprocessed by the Department of Water Resources, WAU, i.e. calibrated and converted to sigma nought,  $\sigma^0$ , and subdivided into smaller scenes. Most of the analysis of the data has been performed by the Institute of Earth Sciences, Free University of Amsterdam.

1994	1995
	02-04
14-05	07-05
24-06	11-06
07-07	11-07
10-07	16-07

Table 4.4: Dates of ERS-1 images that are available

#### 4.4.3 ERS-1 WSC

Windscatterometer data from the ERS-1 satellite has been obtained for five global regions, for the period August 1991 to October 1995 and are available on two CD-ROMs. The filename convention is as follows:

EYYMMDD.KKK

where YY, MM, DD is the year, month and day, respectively and KKK the code for the area as can be delineated from Table 4.5. This table also illustrates the coordinates of the five regions, and the periods of data coverage. In this report, only data from the Scandinavian region are considered.

Site	Coordinates	File Ending	latmax	latmin	lonmax	lonmin	
Scandinavia		sca	70 N	55 N	35 E	10 E	[Apr. 95 - Oct. 95] <sup>+</sup> [Aug. 91 - Mar. 95] <sup>*</sup>
Sahel		sah	20 N	7 S	17 E	3 W	[Apr. 95 - Oct. 95] <sup>+</sup> [Aug. 91 - Mar. 95] <sup>*</sup>
Kalimantan		kal	8 N	5 S	120 E	106 E	[Apr. 95 - Oct. 95] <sup>+</sup> [Aug. 91 - Mar. 95] <sup>*</sup>
Mediterranean		med	48 N	26 N	40 E	10 W	[Apr. 95 - Oct. 95] <sup>+</sup> [Aug. 91 - Mar. 95] <sup>*</sup>
Amazon		ama	15 N	10 S	50 W	80 W	[Apr. 95 - Oct. 95] <sup>+</sup>

<sup>\*</sup> Data for February, 1992 has not been reprocessed yet and is therefore missing.

<sup>+</sup> These data are only for temporary use, they will eventually be updated.

Table 4.5: Available WSC data of the five regions at the Department of Water Resources.

The data is in the form of unformatted binary files consisting of records of 20 integer (2 byte) values that include the date, location, and normalised radar cross section ( $\sigma^0$ ) for the three beams. Incidence and azimuth angles for the three beams are also given.

Full coverage is possible within 4 days, but it should be noted that this may be different during the ice phases, and during periods of extensive SAR imaging.

## Chapter 5

# Preliminary results

### 5.1 Modelling with "Treegrow" of Pine and Spruce trees

There is increasing interest in the use of microwave instruments, such as Synthetic Aperture Radar (SAR), to monitor specific characteristics of forest ecosystems. The analysis of such measured data however, requires the development and validation of theoretical models that can predict microwave scattering from vegetation and soils. To date the validation associated with such backscatter models has been limited, the effort needed to collect and analyse extensive ground truth being one of the principal reasons for the shortage of model/data comparisons. To circumvent this difficulty, this study utilises a tree growth model developed at the University of Wageningen which simulates the growth of typical trees within a forest stand, given information about its general characteristics. This allows for comparisons of modelled and observed backscatter values over large areas without a significant increase in ground truth measurements

#### 5.1.1 Parameterisation of Forest Stands

Using a combination of the field estimates of tree density, tree stand ages from forestry records, and the data from the tree growth model, individual stands can be characterised by number densities and angular distributions of cylindrical branch elements in different layers. A visual representation illustrating three stands considered in this study is shown in Figure 5.1. These modelled sites were two pine stands, (28 and 67 years old) and a 38 year old spruce stand.

The current study has concentrated on stands with dense forest cover to minimise the effect of surface characteristics.

The determination of the layering scheme is dependant upon the characteristics of each forest stand, but are generally one of three categories (each of which is clearly evident in the three cases shown in Figure 5.1):





Figure 5.1: Representative cross-sections of three of the test stands. From left to right they are, stand 18 (67 year old pine), stand 46.1 (38 year old spruce) and stand 21 (28 year old pine).

- 1 layer: (1) Small upright trunks, live branches, needles.
- 2 layer: (1) Small upright trunks, live branches, needles.  
(2) Upright trunks, dead branches.
- 3 layer: (1) Small upright trunks, live branches, needles.  
(2) Upright trunks, dead branches.  
(3) Large upright trunks.

An example of an input file for the UTA model based on these data is shown in Table 5.1.

## 5.2 Forward Backscatter Modelling Using the UTA model

Data from the tree growth model is used to drive the radiative transfer backscatter model and rough surface scattering model developed by Karam et al., (1992) at the University of Texas. This model was developed to simulate the microwave scattering of layered vegetation and is based on an iterative solution of the radiative transfer equation up to the second order to account for multiple scattering within the canopy and between the ground and the canopy. The canopy may be represented by up to three layers, with the branches and needles (or leaves) within each layer being grouped into different sizes each with their own orientation distribution. These scatterers are modelled as randomly positioned finite-length dielectric cylinders. Figure 5.2 shows a visual representation of the stand modelling process (not to scale).

### 5.2.1 Results

The model results were computed at C- and L-band over a range of incidence angles using the simulated stands as input to the scattering model. The model predictions for the total backscatter (given as  $\gamma = \sigma^0 / \cos \theta_i$ ) from the Siggefora

---

sim.in									
2									
d28LC.mul									
d28LC.sct									
d28LC.lf1									
d28LC.lf2									
d28LC.Br1									
d28LC.Br2									
d28LC.sur									
d28LC.att									
.FALSE.									
15.000									
5.300									
1									
18									
42	48	3							
6.73000	4.00000	0.0000							
0.0150000	0.15000	0.2400	0.5000	0.2000					
5	5	0	0						
6.00e-04	3.50e-02	7.0e-01	0.00e+03	0.0e+00	0.0e+00	1.8e+02	9.0e+01	1.0e+00	
6.50e-04	3.50e-02	7.0e-01	0.00e+03	0.0e+00	0.0e+00	1.8e+02	9.0e+01	1.0e+00	
7.00e-04	3.50e-02	7.0e-01	0.00e+03	0.0e+00	0.0e+00	1.8e+02	9.0e+01	1.0e+00	
7.50e-04	3.50e-02	7.0e-01	0.00e+03	0.0e+00	0.0e+00	1.8e+02	9.0e+01	1.0e+00	
8.00e-04	3.50e-02	7.0e-01	0.00e+03	0.0e+00	0.0e+00	1.8e+02	9.0e+01	1.0e+00	
11	10	1	0						
1.25e-03	1.05e-01	6.5e-01	1.53e+01	0.0e+00	2.0e+01	0.9e+02	9.0e+01	1.0e+00	
2.00e-03	2.21e-01	6.5e-01	1.29e+01	0.0e+00	2.0e+01	0.9e+02	9.0e+01	1.0e+00	
4.00e-03	2.83e-01	5.5e-01	3.42e+01	0.0e+00	2.0e+01	0.9e+02	9.0e+01	1.0e+00	
6.00e-03	4.00e-01	5.5e-01	1.84e+01	0.0e+00	2.0e+01	0.9e+02	9.0e+01	1.0e+00	
8.00e-03	5.10e-01	5.5e-01	9.28e+00	0.0e+00	2.0e+01	0.9e+02	9.0e+01	1.0e+00	
1.00e-02	6.34e-01	5.5e-01	8.27e+00	0.0e+00	2.0e+01	0.9e+02	9.0e+01	1.0e+00	
1.60e-02	8.65e-01	5.5e-01	2.09e+00	0.0e+00	2.0e+01	0.9e+02	9.0e+01	2.0e+00	
2.80e-02	1.10e+00	5.5e-01	1.85e+00	0.0e+00	2.0e+01	0.9e+02	9.0e+01	4.0e+00	
6.00e-02	1.64e+00	5.0e-01	1.37e-01	0.0e+00	8.0e+01	1.0e+02	9.0e+01	6.0e+00	
1.10e-01	2.11e+00	5.0e-01	4.03e-02	0.0e+00	0.0e+00	1.0e+01	5.0e+01	4.0e+00	
6.84e-02	3.89e+00	5.0e-01	6.78e-02	0.0e+00	0.0e+00	1.0e+01	5.0e+00	4.0e+00	

---

Table 5.1: An example input file to the backscatter model. The data represent various characteristics of representative cylinders, such as radius, length, angular distribution, etc.

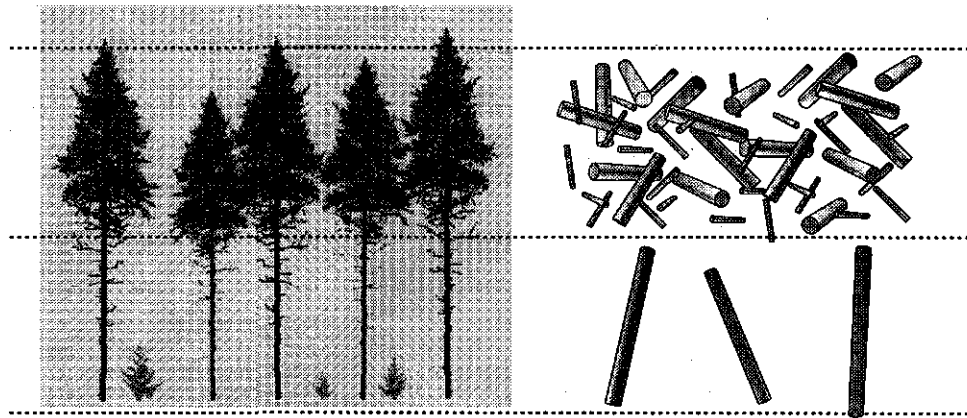


Figure 5.2: Graphical representation of the stand modelling process. Branches are represented as dielectric cylinders (figure is not to scale).

forest stands are shown in Table 5.2 alongside the EMISAR measured values.

For like-polarisation the experimental values are consistently higher than those predicted by the model by up to 3.3 dB for the pine stands and 5.4 dB for the spruce stand. The results for the pine stands are comparable to earlier modelling studies which have encountered similar discrepancies between modelled and measured backscatter [19, 18]. Cross-polarisation values are also underestimated by the model, by 3.5 dB at L-band and as much as 6.7 dB at C-band. These results may be a consequence of the model only being to first order (i.e., multiple scattering is not accounted for in these results).

At C-band the HH and VV experimental values differ by only 0.1 to 0.6 dB indicating that the main scatterers are randomly orientated; i.e. that the needles or the smallest twigs are the main contributors to the backscatter. The model predicts similar results, with only small differences between the like-polarisation values.

At L-band the differences between the like-polarisations are dramatically different, the HH values being generally higher by 1.5 dB or more. While the backscatter model predicts the value of the VV backscatter to within 1.0 dB for most of the stands, it fails to predict the much higher HH values. A likely explanation for this discrepancy, as well as the overall underestimation of the backscatter, may lie in the manner in which the model characterises the needles within the canopy. Unlike in real trees, where the needles are clustered around the smaller branches, the model considers the needles to be evenly distributed throughout the canopy. For the small needles found on Norwegian Spruce (3 cm) and Scots Pine (6 cm) this forms an attenuating cloud rather than a layer of strong scatterers, thus limiting the backscatter signal from the larger branches. A more realistic way of modelling such trees would require representing needle-covered branches by equivalent dielectric cylinders.

### 5.2.2 Summary

We have introduced the use of a tree growth model to provide statistical information about the dimensions and angular distributions of scattering components of Scots Pine and Norwegian Spruce stands within the Siggefora forest. Such data has been used as input to a backscatter model as an alternative to using intensive field data and has been used to predict the total backscatter from three test stands at C and L-band frequencies for three linear polarisation combinations (HH, VV and HV). The model predictions were compared with experimental data from the Danish EMISAR instrument and the differences and similarities were analysed. The simulation results show the model worked well for the Scots Pine stands but were significantly poorer for the Norwegian Spruce.

## 5.3 Inverse modelling of soil moisture

### 5.3.1 Theoretical framework

To describe the microwave scattering from rough surfaces various models have been developed [25][8]. One of the most recent physically based models is the Integral Equation Method (IEM) [9][8] which under certain roughness conditions can be simplified to the Kirchhoff approaches, geometrical optics (GO) and phys-

	Stand number	Description (age)	HH			VV			XP		
			$\gamma_{obs}$	$\gamma_{mod}$	$\gamma_{obs}-\gamma_{mod}$	$\gamma_{obs}$	$\gamma_{mod}$	$\gamma_{obs}-\gamma_{mod}$	$\gamma_{obs}$	$\gamma_{mod}$	$\gamma_{obs}-\gamma_{mod}$
L-Band	1	Pine (66)	-5.9	-8.4	2.5	-7.5	-8.5	1.0	-11.4	-14.7	3.3
	2	Mixed (70)	-5.7	-8.4	2.7	-7.9	-8.0	0.1	-12.2	-14.0	1.8
	3	Spruce (37)	-4.8	-8.1	3.3	-6.5	-8.1	1.6	-10.9	-13.5	2.6
	4	Pine (28)	-6.8	-8.4	1.6	-8.4	-8.4	0.0	-13.4	-14.1	0.7
	5	Pine (27)	-6.3	-8.4	2.0	-5.8	-8.3	2.4	-10.7	-14.2	3.5
	6	Pine (66)	-6.4	-8.4	2.1	-7.9	-8.5	0.5	-12.1	-14.7	2.6
C-Band	1	Pine (66)	-7.9	-9.4	1.5	-8.0	-9.3	1.3	-13.4	-20.1	6.7
	2	Mixed (70)	-7.8	-9.2	1.4	-7.6	-9.1	1.6	-13.7	-17.7	4.0
	3	Spruce (37)	-5.9	-11.2	5.3	-5.8	-11.1	5.4	-11.7	-16.6	4.9
	4	Pine (28)	-8.6	-11.9	3.3	-9.2	-11.4	2.2	-14.3	-18.5	4.2
	5	Pine (27)	-8.4	-10.9	2.5	-8.6	-10.9	2.3	-13.4	-18.6	5.2
	6	Pine (66)	-8.0	-9.4	1.4	-8.5	-9.3	0.8	-13.7	-20.0	6.3

Table 5.2: Comparison of C and L-band observed backscatter with modelled backscatter from Siggefora (observed backscatter from EMISAR July 1995). All values in dB.

ical optics (PO), and the first order small perturbation approach. Hereafter, the inverse IEM model introduced in this paper will be referred to as INVIEM. Examples of other soil moisture retrieval algorithms are the semi-empirical model developed by Oh et al. (1992) [21] and the model by Dubois et al. (1995) [6].

The INVIEM model is applied on an object as well as a pixel basis. The first step was to use the IEM model to describe the backscatter of the various objects and compare them to the backscatter measured by the different sensors. The second step was to apply the IEM model in an inverse way to estimate the soil moisture content and compare it with the available ground truth data. The INVIEM model is in its current form only valid for bare soil surfaces, hence those areas where the influence of vegetation is too strong should be eliminated. For the FOREST-DYNAMO experiment polarimetric data are available. Using the two frequencies (or bands) the scattering classification mentioned in section 5.5.1 can be used to develop a mask to eliminate the pixels with too much vegetation influence. An additional criterion which can be applied is the ratio  $\frac{\sigma_{HV}^{obs}}{\sigma_{HH}^{obs}}$  of cross- and like-polarisation, which should be above a certain threshold. This can be particularly useful when one of the co-polarisation measurements in a band suffers from interference. Consequently, the inverse models were applied to all bands separately. When polarimetric data are not available other (i.e. non-radar) data sources can be used to assess where there is vegetation and where not.

The presence of speckle, inherent to SAR data, is reduced as much as possible by applying a smoothing window that averages the bare soil pixels within that window. Only when the centre pixel of the window was a bare soil pixel and at least three bare soil pixels were present then the average was assigned to the centre pixel, otherwise the centre pixel was masked too. Various sizes of the window have been applied and a window size of  $3 \times 3$  pixels removed most of the speckle influence while retaining much of the spatial information. However, Van Oevelen et al. 1996 [27] showed that when soil moisture is estimated from

$Mv$	$k\sigma$	$kL$	$\epsilon'$	$\epsilon''$	$\theta_{inc}$	$\sigma_{VV}^\circ$	$\sigma_{HH}^\circ$
[-]	[-]	[-]	[-]	[-]	[Rad]	[dB]	[dB]
0.00	0.34	4.49	2.65	0.00	0.4	-16.67	-17.55
0.00	0.79	11.22	2.65	0.00	0.4	-13.57	-13.58
0.00	1.24	17.95	2.65	0.00	0.4	-12.51	-11.60
0.05	0.34	4.49	4.39	0.36	0.4	-13.05	-14.30
0.05	0.79	11.22	4.39	0.36	0.4	-9.94	-10.33
0.05	1.24	17.95	4.39	0.36	0.4	-8.86	-8.35
0.10	0.34	4.49	6.46	0.84	0.4	-11.12	-12.60
0.10	0.79	11.22	6.46	0.84	0.4	-8.00	-8.63
0.10	1.24	17.95	6.46	0.84	0.4	-6.91	-6.64
0.15	0.34	4.49	8.81	1.42	0.4	-9.91	-11.53
0.15	0.79	11.22	8.81	1.42	0.4	-6.78	-7.56
0.15	1.24	17.95	8.81	1.42	0.4	-5.68	-5.58
0.20	0.34	4.49	11.41	2.08	0.4	-9.06	-10.79
0.20	0.79	11.22	11.41	2.08	0.4	-5.93	-6.82
0.20	1.24	17.95	11.41	2.08	0.4	-4.83	-4.84

Table 5.3: An example of a part of a Look Up Table (LUT) for C-band, HH and VV polarisation. Three different roughness cases, one incidence angle, and a soil moisture range from 0.00 to 0.20 with steps of 0.05 is used to generate this table.

SAR data on a pixel by pixel basis the presence of speckle introduces an offset of the actual soil moisture value on a field average basis. When field averaged backscatter data were used this offset is not introduced. Thus care has to be taken when estimating soil moisture on a pixel basis.

Roughness case	C		L	
	$k\sigma$	$kL$	$k\sigma$	$kL$
1	2.4	18.92	0.56	4.41
2	1.18	8.45	0.27	1.97
3	0.85	1.92	0.19	0.45

Table 5.4: Surface roughness parameters for the three selected cases used in the INVIEM model for FOREST-DYNAMO.

The INVIEM model uses a Look Up Table (LUT) of IEM simulation results (Table 5.3). This comprises a range of volumetric soil moisture content values  $Mv$ , with  $0 < Mv < 0.45$  and a step size of 0.05, and a range of incidence angles ( $\theta_{inc}$ ), covering the variation in the image. For these ranges simulations were made for a number of surface roughness conditions covering the extremes of  $k\sigma$  and  $kL$  in the reference field data set (4.14.2). The values of the surface roughness cases used for the INVIEM model are given in Table 5.4. For the various frequencies and the different types of soil several soil mixing models have been applied to relate the complex soil dielectric constant to the soil moisture content [5][12][30]. For each frequency band and polarisation combination, limited to HH and VV polarisation, the soil moisture extremes, related to the different roughness conditions, are determined by linear interpolation for the appropriate incidence angle and measured backscatter value. Since this interpolation can be done for HH and VV the range of possible solutions is limited

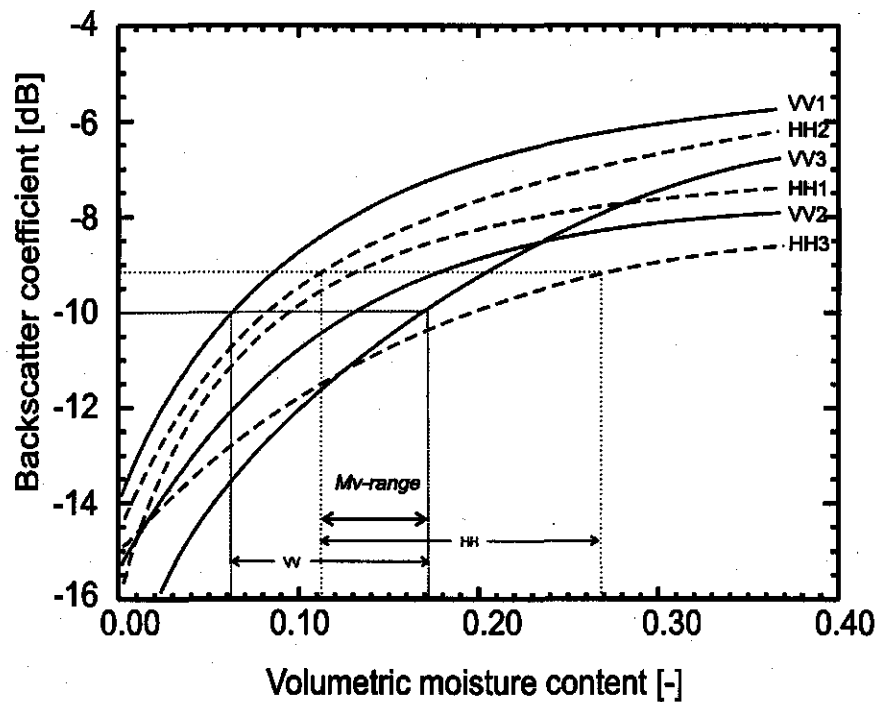


Figure 5.3: Graphical representation of the Look Up Table generated with the IEM model and the inversion using the INVIEM model.

to the overlap of the soil moisture ranges resulting from the backscatter of both polarisation (Figure 5.3). The whole procedure is done for both bands, i.e. C- and L-band of the EMISAR. Thus, the INVIEM model estimates a range of soil moisture values for an assumed range of roughness conditions using one single backscatter value. The HH and VV inversions are combined to narrow this range (Figure 5.3). In this study all the estimates are used and averaged to give a “average” estimate. Depending upon the roughness classes, the sensitivity of the backscatter on soil moisture content as predicted by the IEM model decreases with increasing soil moisture content (Figure 5.3) which can result in large ranges of soil moisture contents when the INVIEM is applied.

### 5.3.2 Results

The soil moisture has been estimated for the days that the available EMISAR data coincided with the ground truth measurements. These were two days in June of 1995. The results of the comparison of estimated soil moisture with the measured soil moisture content along the transects, indicated as track A to F, are summarised in Tables 5.5 and 5.6.

The same transects are also represented in graphical form in Figures 5.4, 5.5 and 5.6. The overall comparison shows that the EMISAR soil moisture estimates in general underestimate the measured soil moisture content. This can be contributed to the fact that the IEM model doesn't account for periodicity.

Track	A		B		C		D		E		F	
Angle	20	45	20	45	20	45	20	45	20	45	20	45
TDR												
avg	20.07	19.19	24.66	27.63	18.49	24.54	22.89	26.64	16.15	23.53	22.83	27.94
st.dev	4.68	6.53	3.35	4.07	6.42	6.44	3.29	4.54	5.88	5.08	4.44	4.85
L-band												
avg	14.19		14.36		17.45		18.22		14.59		15.35	
st.dev	2.72		2.14		2.84		3.28		2.29		1.99	

Table 5.5: TDR volumetric soil moisture content compared with L-band EMISAR estimates using the INVIEM model. Data is taken on June 5, 1995.

Track	A		B		C		D		E		F	
Angle	20	45	20	45	20	45	20	45	20	45	20	45
TDR												
avg	15.78	19.93	15.67	22.28	16.23	23.25	14.36	22.95	16.42	23.87	17.79	25.66
st.dev	3.58	6.04	4.16	4.42	3.49	5.53	3.99	3.27	3.97	4.62	4.08	3.63
C-band												
avg	11.49		11.27		14.44		15.38		12.28		12.74	
st.dev	3.76		3.91		4.33		4.49		4.07		4.32	

Table 5.6: TDR volumetric soil moisture measurements compared with C-band EMISAR estimates. Data is taken on June 6, 1995.

or anisotropy in the surface roughness characteristics and therefore in those case gives a lower backscatter coefficient than actually measured. Furthermore, there might be an inconsistency between measured surface roughness and the way it is represented in the model. The in situ measured RMS height and correlation length does not necessary resembles the for the radar backscattering relevant surface roughness. The backscattering is likely to be caused by a smoother subsurface.

Both the C- and L-band estimates seem to agree better with the soil moisture measurements taken with the TDR rod at a shallower angle with respect to the surface, resulting in a measurement depth of about 2-3 cm. Most estimates are within 5% of the measurements. Since the standard deviation of the measurements lies mostly between 4 and 6% these results are acceptable. Only the comparison with L-band on June 5 for track A, B and F are outside the 5% range. No particular reason could be found for these exceptions.

## 5.4 Inversion of Scandinavian WSC Data

### 5.4.1 Forward Model

In endeavouring to retrieve geophysical parameters from the WSC data, it is necessary to develop a forward model that accounts for those effects considered important at C-Band VV and which are relevant for the region under observation. In our treatment, the resolution cell is represented by an equivalent surface consisting of a combination of only two surface types: dense, homogeneous veg-



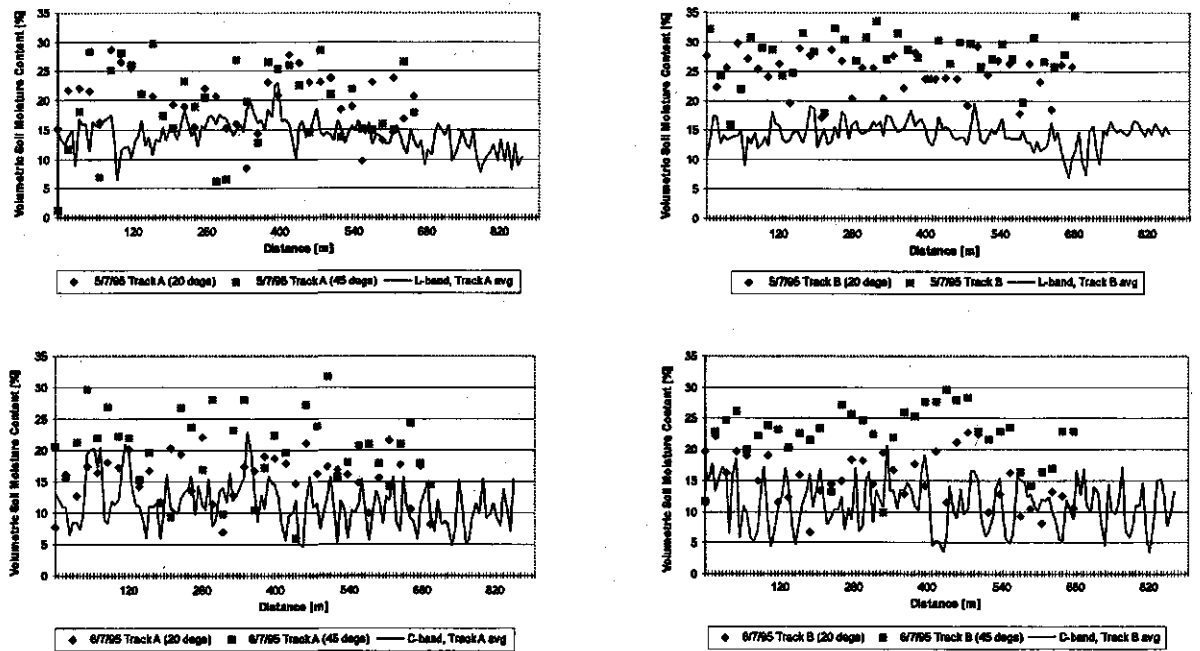


Figure 5.4: EMISAR C- and L-band Soil moisture estimates using the INVIEM model compared with TDR measurements for tracks A and B.

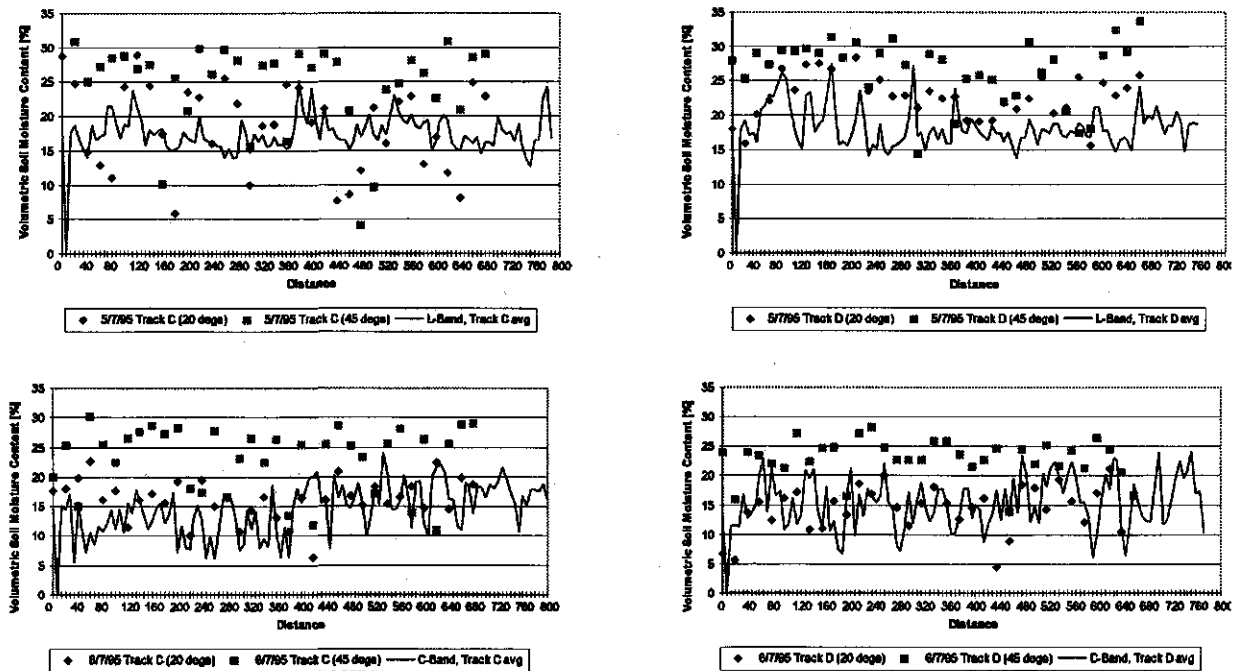


Figure 5.5: EMISAR C- and L-band Soil moisture estimates using the INVIEM model compared with TDR measurements for tracks C and D.

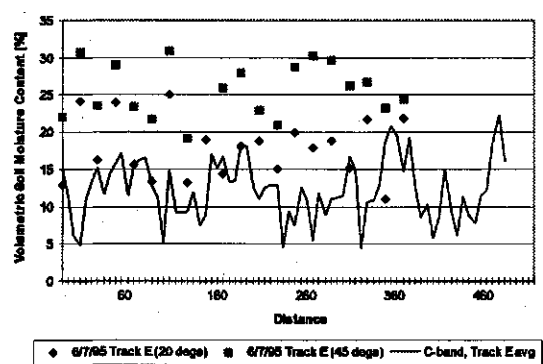
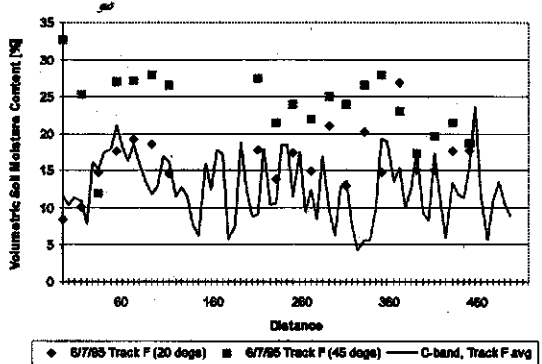
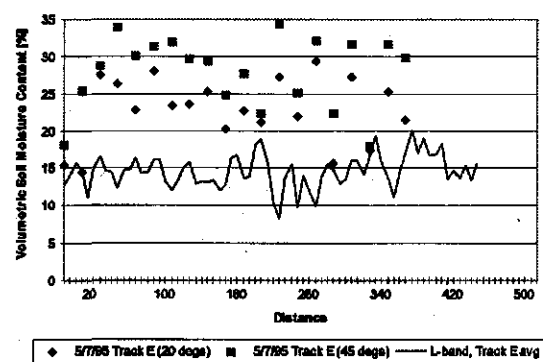
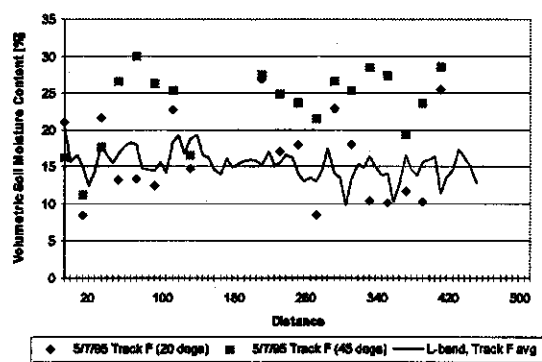


Figure 5.6: EMISAR C- and L-band Soil moisture estimates using the INVIEM model compared with TDR measurements for tracks E and F.

etation (pure volume scattering) with a fractional surface area denoted by  $C$ , and bare soil with effective (homogeneous) roughness and dielectric properties (surface scattering). The total backscatter is therefore considered to be an incoherent sum of three backscattering mechanisms: these are (vegetation) volume scattering, surface scattering from the bare soil layer, and specular (double-bounce) reflection between the trunk and ground. In addition, a fourth term may be added which accounts for all other contributions not included in the first three. Since this term may include contributions from such features as highly specular surfaces, its overall effect may be to reduce the total observed backscatter, so that it may be considered to be a random error on the forward model calculation.

Specific models are adopted for each component separately, and their contributions are calculated for an incidence angle  $\theta_i$  and azimuth angle  $\phi_i$ , and are summed incoherently so that

$$\sigma^0(\theta_i, \phi_i) = C\sigma_{cover}^0 + [1 - C]\sigma_{bare}^0 + \sigma_{double}^0 + \sigma_{other}^0 \quad (5.1)$$

where,

$\sigma^0(\theta_i, \phi_i)$  = scattering coefficient measured at the WSC,

$C$  = equivalent fractional vegetation cover,

$\sigma_{cover}^0$  = contribution from equivalent vegetation cover,

$\sigma_{bare}^0$  = contribution from equivalent bare soil,

$\sigma_{double}^0$  = contribution from double-bounce scattering,

$\sigma_{other}^0$  = contribution from other sources.

The individual contributions may be modelled in a number of different ways, from simple empirical models to elaborate radiative transfer models. The choice is dependant upon the specific problem at hand, and is influenced by such factors as the availability and reliability of ground truth, or the parameters one wishes to determine from the measurements. In the current study, the nature of the investigation is to monitor an area with limited ground data and with a high degree of variation in surface parameters. A simple approach is therefore adopted in order to illustrate the applicability of this method, and to highlight the potential of using WSC data. In the current study,  $\sigma_{cover}^0$  was kept constant (such that  $\sigma_{cover}^0 / \cos \theta_i = -6.0$ ) and

$$\sigma_{bare}^0 = \frac{|R_g|^2}{2s^2 \cos^4 \theta_i} \exp(-\tan^2 \theta_i / 2s^2) \quad (5.2)$$

$$\sigma_{double}^0 = T R_1 R_2 \sin^2(\theta_i + 45^\circ). \quad (5.3)$$

#### 5.4.2 WSC Inverse Model

In many physical problems the forward model can be expressed in the simplified linear quadrature form

$$\mathbf{y} = \mathbf{K}\mathbf{x} + \boldsymbol{\epsilon}_y \quad (5.4)$$

where the elements of the vector  $\boldsymbol{\epsilon}_y$  represent the error or noise associated with each measurement  $y_i$  and  $\mathbf{K}$  now represents the forward model (Equation 5.1) as a kernel matrix which characterises the measurements made by the instrument (represented by the vector  $\mathbf{y}$ ) and describes how they depend on the state of

the illuminated surface region (represented by the vector  $\mathbf{x}$ ). In the problem at hand, the surface state vector is defined as

$$\mathbf{x} = \begin{bmatrix} C \\ s \\ T \\ |R_g|^2 \end{bmatrix}$$

The retrieval, or inverse, problem then requires deducing the best estimate of the state  $\mathbf{x}$  of the observed ground area from a set of measurements  $\mathbf{y}$ . In the case of the WSC, there are only three measurements to determine four parameters, so that *a priori* information is required to constrain the solution.

A common approach to the inverse problem is to assume that all the statistical distributions within the problem are Gaussian so that an Optimal Estimation (or Maximum Likelihood) method may be employed [23]. Such a method allows for the use of the *a priori* information to constrain the final solution and gives the optimum solution  $\hat{\mathbf{x}}$  as

$$\hat{\mathbf{x}} = \mathbf{x}^{(0)} + \mathbf{S}_x \mathbf{K}^T (\mathbf{K} \mathbf{S}_x \mathbf{K}^T + \mathbf{S}_\epsilon)^{-1} (\mathbf{y} - \mathbf{y}^{(0)}) \quad (5.5)$$

where,  $\mathbf{x}^{(0)}$  represents the *a priori* state vector with its associated error covariance matrix  $\mathbf{S}_x$ ,  $\mathbf{S}_\epsilon$  is a diagonal measurement error covariance matrix, with elements equal to  $\epsilon_y$ , and  $\mathbf{y}^{(0)} = \mathbf{K} \mathbf{x}^{(0)}$ .

An alternative interpretation is to consider the *a priori* information as a *virtual measurement* with mean  $\mathbf{x}^{(0)}$  and error covariance  $\mathbf{S}_x$ . The normal rules for combining measurements [14, 23] then give Equation 5.5 directly. The covariance  $\hat{\mathbf{S}}$  of the estimate  $\hat{\mathbf{x}}$  is then

$$\hat{\mathbf{S}} = \mathbf{S}_x - \mathbf{S}_x \mathbf{K}^T (\mathbf{K} \mathbf{S}_x \mathbf{K}^T + \mathbf{S}_\epsilon)^{-1} \mathbf{K} \mathbf{S}_x \quad (5.6)$$

The diagonal of the solution covariance matrix contains the variances, or squares of standard deviations, of the individual components of the solution  $\hat{\mathbf{x}}$  and thus gives a measure of accuracy of the solution.

### 5.4.3 Results

The ERS-Windscatterometer retrieval algorithm was applied to the whole of Scandinavia, with the Nopex region used as a testing area for the algorithm. Temporal variations of surface parameters within this area are unpredictable, with rainfall, snow, frost, open water, and larger agricultural areas all contributing to variations in the backscattered signal. Figures 5.7 (a) to (f) show the results of applying the retrieval algorithm to the WSC data over Scandinavia for January and July 1995, and shows pairs of percentage vegetation cover, reflectivity and RMS slope.

The overall spatial variation of the vegetation cover follows the expected patterns, with vegetation dropping to a minimum in the Tundra areas of the North and in the mountains. The seasonal variability also follows the expected pattern, with the July retrievals showing more vegetation coverage and, in the Tundra, a higher reflectivity than the frozen soils in winter.

To assess the validity of the retrieval algorithm for temperate regions, a subset of WSC data was studied that contained only those measurements made within

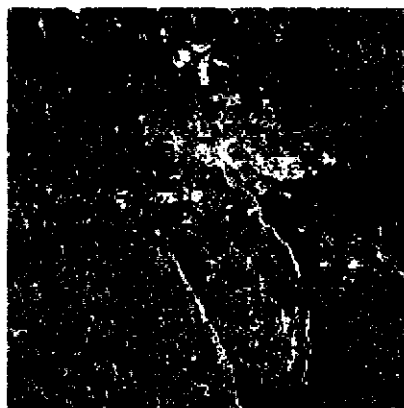


Figure 5.8: Multi temporal ERS-1 SAR image of the NOPEX test area. The generally colourless areas are coniferous forest.

a 1 degree test area near Uppsala, Sweden, coinciding with the NOPEX test area. Multi-temporal ERS-1 SAR data (a colour composite of which is shown in Figure 5.8) was used to perform a maximum likelihood classification of general land-cover types within this area, giving the following proportional land cover values:

forest	49 %
agriculture	19 %
open water	15 %
urban	9 %
other	8 %
unclassified	0 %

Within the framework of the current model, the retrieved vegetation cover would therefore be expected to lie within the range 49% (bare, or snow covered agricultural fields) to 68% (maximum vegetation cover on agricultural fields). In Figure 5.9 we show the temporal variation of the retrieved percentage vegetation cover and reflectivity for the NOPEX test site. The error bars (not shown for reflectivity) indicate the estimated uncertainty on the retrieved values.

The seasonal trends of both parameters are as expected, with low vegetation and higher reflectivity in the winter, contrasting with the high vegetation cover and low reflectivity in the summer. The expected range of percentage cover is also indicated on the figure, and it is clear that the majority of the retrieved values fall within this range. The general trend towards underestimation of the vegetation cover is a consequence of defining -6.0 dB to be the maximum expected backscatter.

If data for a whole month is used to retrieve vegetation cover, a similar trend is observed. Figure 5.10 shows the measurements and subsequent modelled response using the retrieved parameters, for two months in 1995: January and June. The seasonal variation is quite apparent between the two data sets, and the retrieved vegetation cover was 38% and 65% for January and June respectively, again, showing good agreement with the expected results.

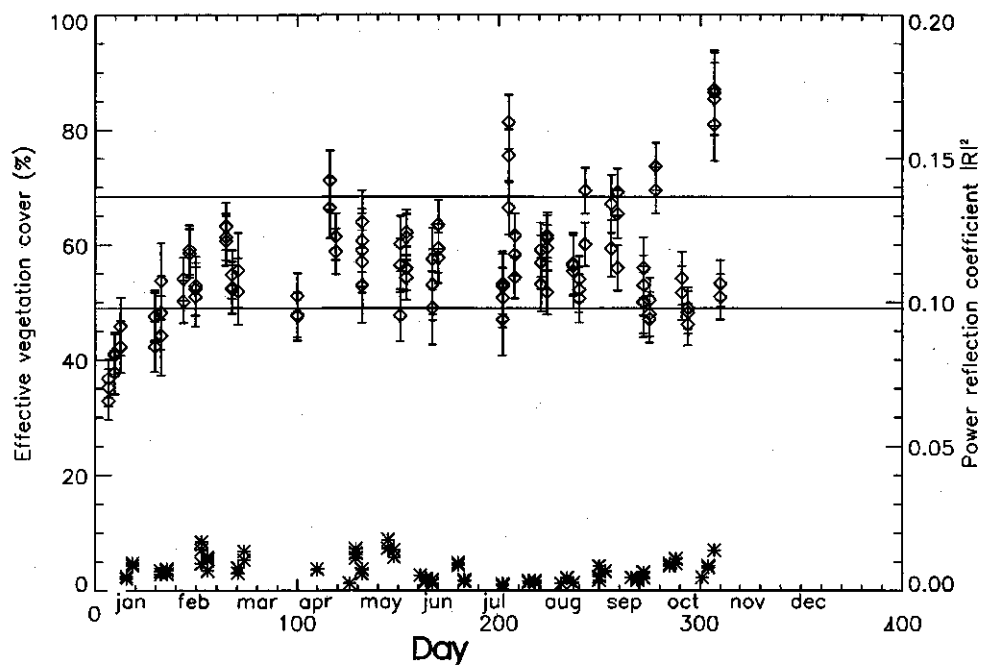


Figure 5.9: The temporal variation of the retrieved percentage vegetation cover and reflectivity for the Nopex test site. The error bars (not shown for reflectivity) indicate the estimated uncertainty on the retrieved values. The horizontal lines indicate the estimated range of vegetation cover from analysis of SAR data of the area.

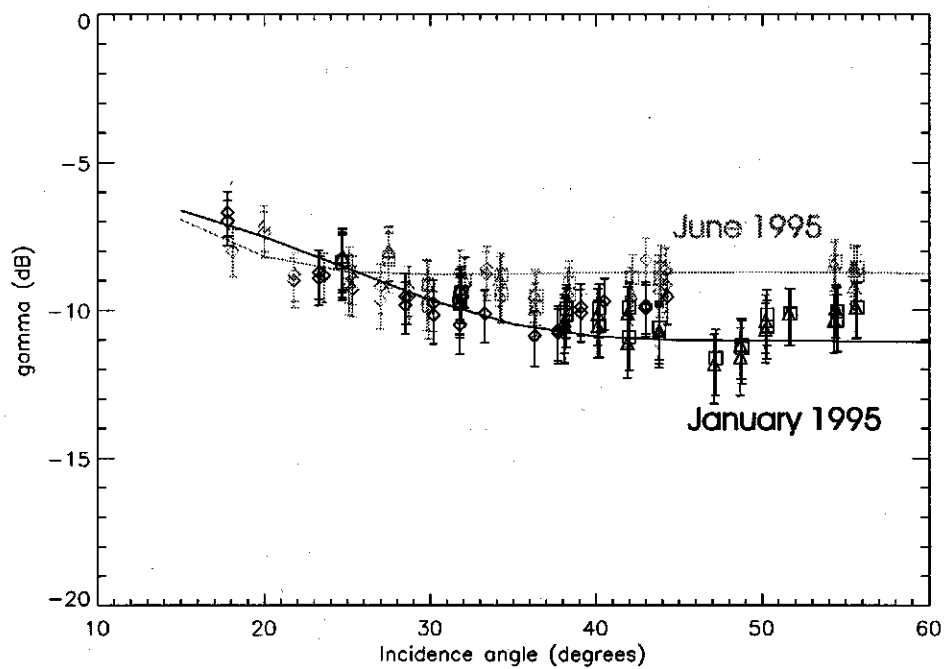


Figure 5.10: Measurements and subsequent modelled response using the retrieved parameters over the NOPEX test area, for two months in 1995: January and June. The seasonal variation is quite apparent between the two data sets, and the retrieved vegetation cover was 38% and 65% for January and June respectively showing good agreement with the expected results.

## 5.5 Classification and segmentation

### 5.5.1 Classification of scattering mechanisms

For soil moisture estimation but also for other purposes, it can be important to identify those areas in an image that are influenced by vegetation cover. Currently no appropriate and simple models that describe the vegetation influence are available. However, it is possible to establish the pixels for which the effect of vegetation is minimal and hence, in the case of soil moisture retrieval the inversion can yield reliable soil moisture estimates. To identify vegetated areas one can use groundtruth data and/or polarimetric radar data and/or optical data. For optical data under cloud free conditions the use of vegetation indices is appropriate to identify areas with low vegetation cover, i.e. low vegetation index value. When polarimetric radar data are available it is possible to determine if a pixel is influenced by vegetation by establishing the *dominant scattering mechanism* from the polarimetric scattering behaviour by comparison with simple classes of scattering such as even/odd number of reflections, and diffuse scattering [7][28]. Odd number reflections occur when the radar signal is reflected only once before it returns to the radar, which is often true for slightly rough surfaces of water bodies, very dense vegetation and bare soil. Even number reflection occurs when the radar signal is reflected twice and then directed back to the sensor, e.g. from dihedral corner reflectors, sparse forest or buildings. Diffuse scattering occurs when the radar signal exhibits multiple scattering interaction and strong depolarisation. This type of scattering can be observed for vegetation. For the higher frequencies ( $f > 5$  GHz) dense vegetation can result in the same type of scattering behaviour as a rough surface. Using multi-frequency SAR data this problem can be reduced since at L-band or even lower frequencies this behaviour can most likely not be observed.

An alternative criterion which can be applied to determine where the vegetation influence is minimal is the ratio of cross- and like-polarisation, i.e.  $\frac{\sigma_{HV}^0}{\sigma_{HH}^0}$ , or  $\frac{\sigma_{HV}^0}{\sigma_{VV}^0}$ , which should be above a certain threshold, e.g. -11 dB [6].

### 5.5.2 Results

The scattering mechanism classification was applied on both C-, and L-band (Figures 5.11,5.12) EMISAR data from 5 and 6 July, 1995 at the Fjärdhundra site. Notice that in L-band much more even scattering (double bounce) is observed, indicating scattering between ground surface and vegetation. The areas with no significant vegetation influence should show odd scattering in both C-, and L-band. By combining the two images it can be concluded that there is significant vegetation cover during these two overpasses of the EMISAR. For soil moisture retrieval the areas which are 'Red' in both images should give the best retrieval results. When vegetation is in the senescent stage or very dry it has a low permittivity, hence the vegetation becomes more transparent for microwaves, in particular for the longer wavelengths such as L-band.



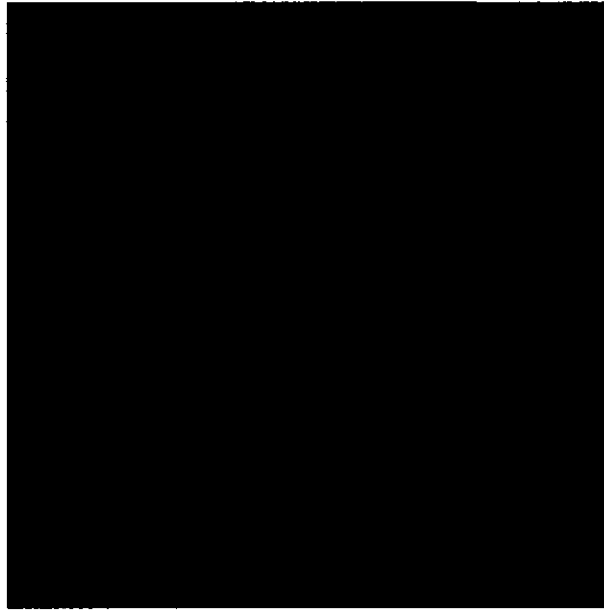


Figure 5.11: C-band scattering classification image of EMISAR data at the Fjärdhubdra site where Red is odd scattering, Green is diffuse scattering and Blue is even scattering.

### 5.5.3 Segmentation

<sup>1</sup>

Segmentation is the automated process to define homogeneous regions that differ statistically from adjacent regions. Most segmentation algorithms use single channel SAR data. The algorithm used here is applicable on multichannel data. The differences in regions may exist in one channel but also in all of the channels. The multichannel approach can be applied to multi-temporal, multi-frequency as well as multi-polarimetric data.

Given a multi-channel image the simplest way of segmenting it is to separately segment each channel and then recombine the results. This problem leads to registration problems and makes no use of any structural correspondence between channels to improve feature detection. The registration problem arises due to the different speckle realisations in each channel causing features to be randomly offset. The alternative approach is to segment the multi-channel images as a single entity.

The single-channel approach involves an iterative process of multi-scale edge detection and segment growing; detected edges are used to limit segment growing; the resulting segmentation is then used to generate a more accurate edge map and in turn an improved segmentation. After each iteration the average contrast of segments is measured, and iteration continues while the average contrast decreases.

---

<sup>1</sup>This section is entirely based upon [2]



Figure 5.12: L-band scattering classification image of EMISAR data at the Fjärdhundra site, where Red is odd scattering, Green is diffuse scattering and Blue is even scattering.

### Edge detection

The algorithm detects edges using a multi-scale gradient operator with thresholding adapted to window size and local standard deviation. This choice of edge detector is based on four criteria: it must be able to 'learn' from the previous segmentation; it must generate a constant false alarm rate; the probability of false alarm (PFA) must be selectable; and it must be possible to detect both low and high contrast edges without causing 'edge thickening'.

### Segment growing

Detected edges are used to limit a segment growing stage. Segments are grown by fitting discs inside regions where no edges have been detected. Discs of diameter 64, 32, 16, 8, 4, 2 and 1 pixels are fitted in order of decreasing size. All the discs of a given size which overlap or abut are merged to form a single segment. Where a segment defined in terms of discs all of the same size overlaps or abuts segments defined in terms of larger discs, the segment is first reduced by discarding the pixels in the overlap, then is merged with the neighbouring segment with the closest mean value.

### Halting the segmentation process

Each segment growing stage is followed by calculation of the average contrast, defined as:

$$\text{average contrast} = \sum_{k=1}^m \frac{n_k \sigma_k^2}{n \mu_k^2}$$

where  $m$  is the number of segments,  $n_k$ ,  $\mu_k$  and  $\sigma_k$  are the area in pixels, mean and standard deviation of segment  $k$ , and  $n$  is the total number of pixels in the image. As segmentation improves the average contrast would be expected to decrease to a limiting value defined by the number of looks. Iteration halts when there is an increase in the average contrast from one iteration to the next. The previous segmentation is then output.

### Multi-channel operation

For multichannel operation we require a single segment labelling to be generated from a multi-channel input. This is achieved by edge detecting in all channels simultaneously, and then thresholding the root mean square (RMS) value of the normalised gradient calculated in all channels. This produces a single edge map which is used as the basis for segment growing. Merging of discs is based on a RMS measure of the difference between the mean value of discs in each channel. After each iteration the average contrast is calculated in each channel. Iteration halts when there is an increase in the RMS average contrast.

### Post processing

After segmentation we can test whether any given segment boundary represents an edge in all or only some channels. For each channel, the existence of an edge is checked by calculating the probability that the segments on either side of the edge share the same mean intensity. This is equivalent to finding the probability that the strength of the edge arose simply from speckle. Edges for which this probability exceeds the PFA used for edge detection are deleted.

## 5.5.4 Results

For the Siggefora test site the segmentation algorithm has been applied to see if different forest stands can be delineated (Figures 5.13 and 5.14). Features such as roads, lakes and rock outcrops can easily be discerned. The clearcut for the powerlines is also easy to be seen. The differentiability between forest stands is not as clear. The segmentation algorithm clearly identifies more heterogeneous regions as one would expect from the forest stand map (Figure 5.1). Also the C-band segmentation shows more contrast than L-band. However, this doesn't automatically mean better delineation of forest stands.

## 5.5.5 Classification of segmented EMISAR data

Using a combination of three channels from the segmentation results (L-HH, L-VV and C-VV) a supervised maximum likelihood classification was performed using IDL-ENVI. A simple set of classes were chosen on the basis of species and age, using data from the Swedish Forestry Service. The results are shown in

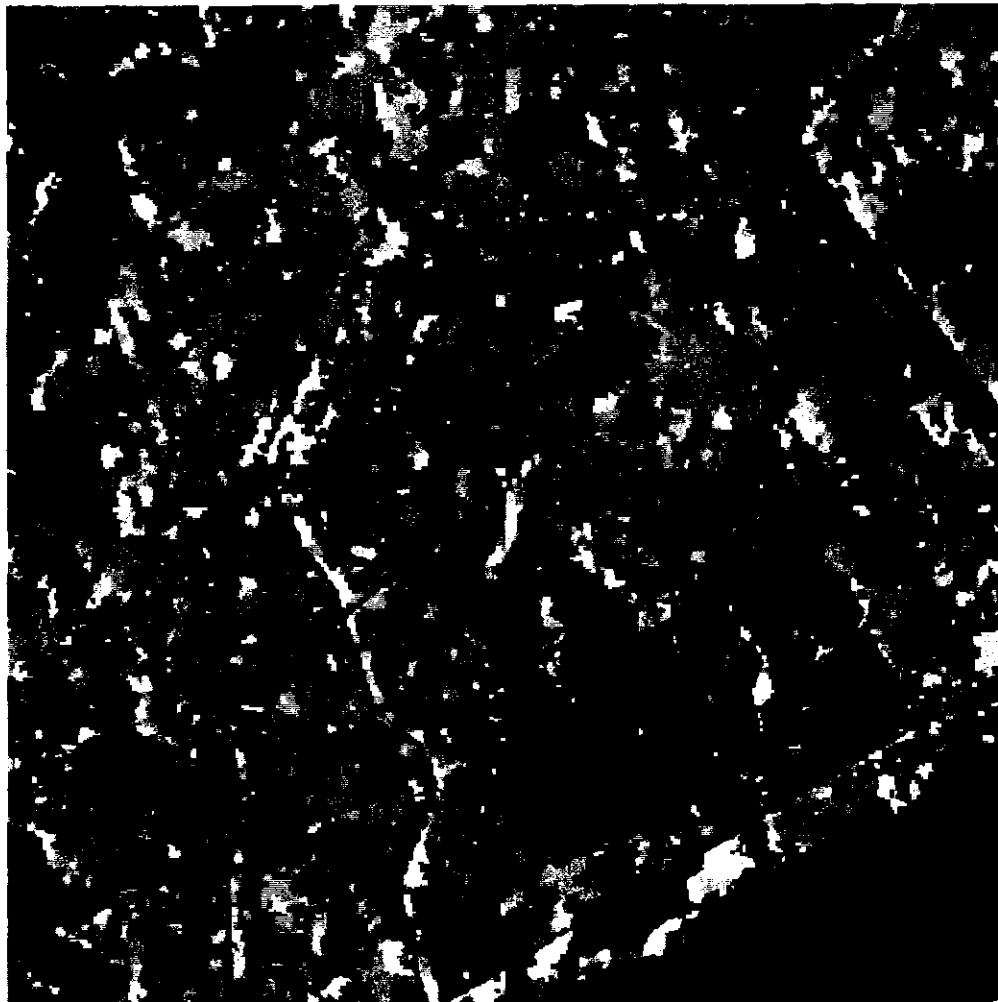


Figure 5.13: Segmentation result using EMISAR C-band data for the Siggefora test site.

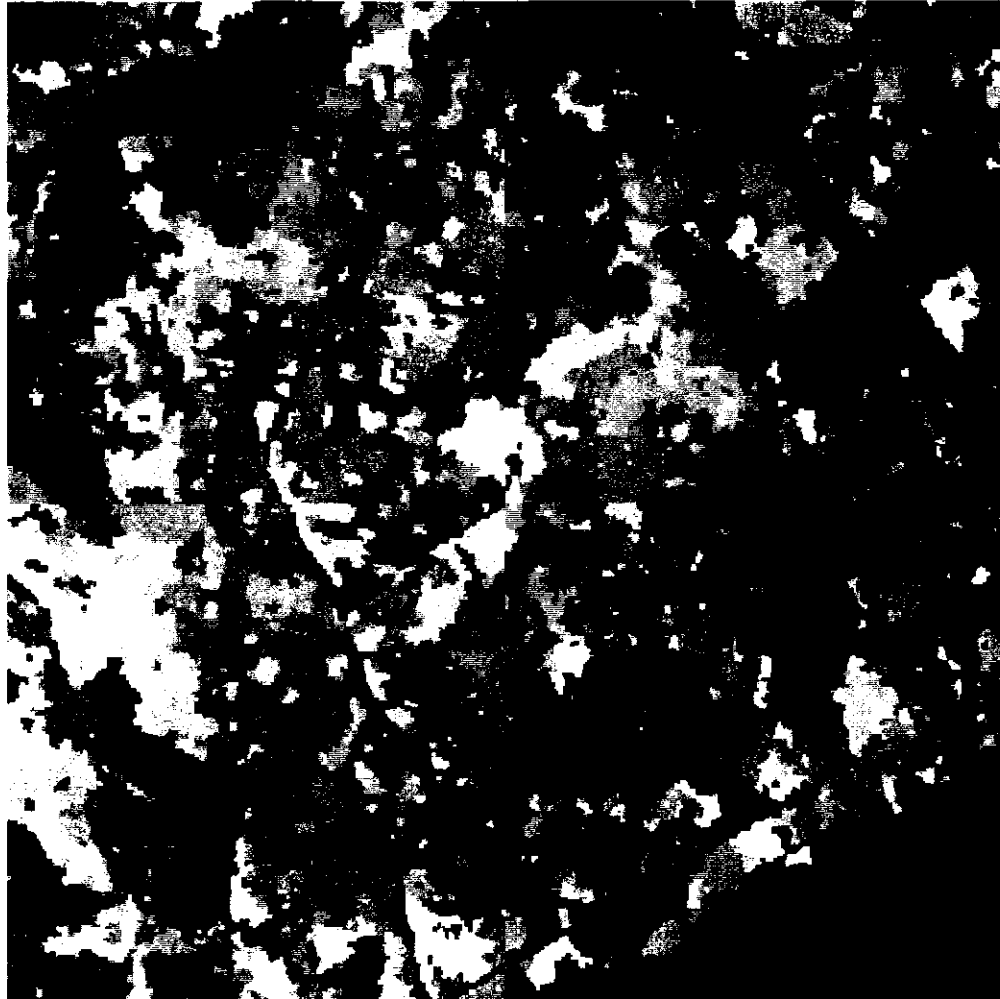


Figure 5.14: Segmentation result using EMISAR L-band data for the Siggefora test site.

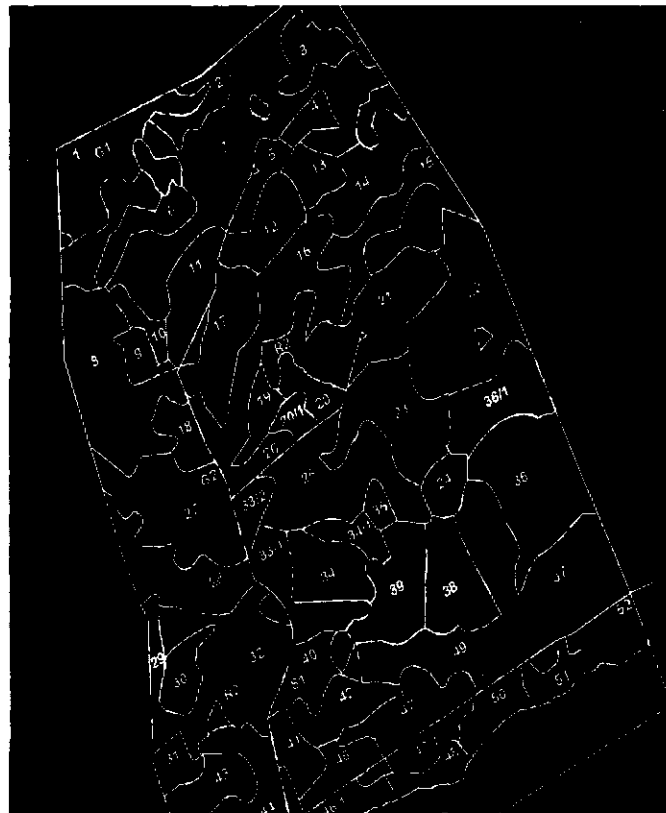


Figure 5.15: A segmentation classification image with the stand borders overlaid.

Figure 5.15, with the forest stand borders overlaid. Areas of clear cut and open water (black) are clearly identified, as are areas of very young growth (less than 15 years old, shown in white). Very few of the classes identify discrete areas comparable to the mapped stands. Apart from the clear cut and young stands, the only other stand borders that are apparent in the classification image are those corresponding to young (<60 years) pine stands: 21, 25, 37, 41, 42 and 49. However, most stands, including the older pine stands, are hardly differentiable. This is likely due to the fact that a number of different stand parameters effect the measured backscatter since they can individually influence the nature of the scattering elements as well as their density and distribution within the tree canopy. Factors such as tree density, tree species concentration and tree age, can all have an influence. The determination of stand "classes" is therefore a fruitless task, but rather more effort should be directed towards determining the properties of the scattering elements.

## Acknowledgements

The work presented in this report resulted from contributions of too many people to mention. The authors are especially thankful for the contributions of Peter Leersnijder, Chris Varekamp and Martin Vissers. Jorgen Dall is acknowledged for his work regarding the EMISAR processing. ESA is acknowledged for making it possible to obtain ERS-1 and EMISAR data. The remote sensing group co-ordinator Ad van de Griend and Jan de Ruyter are thanked for their help with practical matters in the field and their overall co-ordination of the FOREST-DYNAMO project.

# Bibliography

- [1] H.J. Bolle and B. Streckenbach. The ECHIVAL Field Experiment in a Desertification threatened Area. Technical report, EFEDA-Secretariat, Free University of Berlin, 1992. First Annual Report to EC.
- [2] R.G. Caves and S. Quegan. The role of segmentation in multi-channel sar image analysis. pages 1171–1175, 1996.
- [3] J. Dall, S.N. Madsen, H. Skriver, S.S. Kristensen, and E.L. Christensen. EMISAR deployment in the EMAC'94 campaign june 23, 1994, for the NOPEX project at Uppsala, Sweden. Technical report, 1995.
- [4] S. Dasberg and F.N. Dalton. Time domain reflectometry field measurements os soil water content and electrical conductivity. *Soil Sci. Soc. Am. J.*, 49:293–297, 1985.
- [5] M.C. Dobson, F.T. Ulaby, M. Hallikainen, and M. El-Rayes. Microwave dielectric behaviour of wet soil. Part II: Dielectric mixing models. *IEEE Trans. Geosci. Remote Sensing*, 23(1):35–46, 1985.
- [6] P.C. Dubois, J.J. van Zyl, and E.T. Engman. Measuring soil moisture with imaging radars. *IEEE Trans. Geosci. Remote Sensing*, 33(4):915–26, July 1995. Corrections in: 33(6):1340, November, 1995.
- [7] D.L. Evans, T.G. Farr, J.J. van Zyl, and H.A. Zebker. Radar polarimetry: analysis tools and applications. *IEEE Trans. Geosci. Remote Sensing*, 26(6):774–789, November 1988.
- [8] A.K. Fung. *Microwave scattering and emission models and their applications*. Artech House, Norwood, 1994.
- [9] A.K. Fung, Z. Li, and K.S. Chen. Backscattering from a randomly rough dielectric surface. *IEEE Trans. Geosci. Remote Sensing*, 30(2):356–369, March 1992.
- [10] J.P. Goutorbe, T. Lebel, A. Tinga, P. Bessemoulin, J. Brouwer, A.J. Dolman, E.T. Engman, J.H.C. Gash, M. Hoepffner, P. Kabat, Y.H. Kerr, B. Monteny, S. Prince, F. Said, P. Sellers, and J.S. Wallace. HAPEX-Sahel: a large scale study of land-atmosphere interactions in the semi-arid tropics. *Annales Geophysicae*, 12:53–64, 1994.
- [11] S. Halldin, L. Goyttschalk, A.A. van de Griend, S-E. Gryning, M. Heikoneimo, U. Högström, A Jochum, and L-C. Lundin. Science plan for nopex. Technical Report 12, NOPEX Central Office, 1995.



- [12] M.T. Hallikainen, F.T. Ulaby, M.C. Dobson, M.A. El-Rayes, and L. Wu. Microwave dielectric behaviour of wet soil. Part I: Empirical models and experimental observations. *IEEE Trans. Geosci. Remote Sensing*, 23(1):25–34, January 1985.
- [13] T.J. Heimovaara and W. Bouten. A computer controlled 36-channel time domain reflectometry system for monitoring soil water contents. *Water Resources Research*, 26(10):2311–2316, October 1990.
- [14] J.T. Houghton. *The Physics of Atmospheres*. Cambridge University Press, Cambridge, 1977.
- [15] R.P. Leersnijder. *PINOGRAM: a pine growth area model*. PhD thesis, Wageningen Agricultural University, The Netherlands, May 1992.
- [16] L-C. Lundin and S. Halldin. Nopex-experimental plan: part 2. Technical report, NOPEX Central Office, 1994.
- [17] L-C. Lundin and S. Halldin. Nopex-experimental plan: part 1. Technical report, NOPEX Central Office, 1994.
- [18] Roger H. Lang Mostafa A.Karam, Adrian K. Fung and Narinder S. Chauhan. A microwave scattering model for layered vegetation. *IEEE Transactions on Geoscience and Remote Sensing*, 30(4):767–784, July 1992.
- [19] Roger H. Lang Narinder S. Chauhan and K. Jon Ranson. Radar modeling of a boreal forest. *IEEE Transactions on Geoscience and Remote Sensing*, 29(4):627–637, July 1991.
- [20] J.A. Ogilvy. *Theory of wave scattering from random rough surfaces*. IOP Publishing Ltd, Redcliffe Way, Bristol, BS1 6NX, 1990.
- [21] Y. Oh, K. Sarabandi, and F.T. Ulaby. An empirical model and an inversion technique for radar scattering from bare soil surfaces. *IEEE Trans. Geosci. Remote Sensing*, 30(2):370–381, March 1992.
- [22] W.H. Press, S.A. Teukolsky, W.T. Vetterlin, and B.P. Flannery. *Numerical Recipes in FORTRAN. The art of scientific computing*. Cambridge University Press, 2nd edition, 1992.
- [23] C. D. Rodgers. Retrieval of atmospheric temperature and composition from remote measurements of thermal radiation. *Reviews of Geophysics and Space Physics*, 14(4):609–624, November 1976.
- [24] G.C. Topp, J.L. Davis, and A.P. Annan. Electromagnetic determination of soil water content: measurement in coaxial transmission lines. *Water Resources Research*, 16(3):574–582, June 1980.
- [25] F.T. Ulaby, R.K. Moore, and A.K. Fung. *Microwave Remote Sensing: active and passive*, volume III From theory to applications. Artech House, Norwood, 1986.
- [26] A.A. van de Griend, D.H. Hoekman, Y.H. Kerr, P. Pampaloni, and H. Sogaard. Forest environmental dynamics monitoring and climate research. Annual report to the ec 1994–1995, Institute of earth sciences, Free University Amsterdam, May 1995.

- [27] P.J. van Oevelen, D.H. Hoekman, and R.A. Feddes. Sensitivity analysis of the estimation of areal soil water content through radar remote sensing during HAPEX-Sahel and EFEDA-Spain. *Proc. Upscaling Workshop, Wallingford, UK*, 1996.
- [28] J.J. van Zyl. Unsupervised classification of scattering behavior using radar polarimetry data. *IEEE Trans. Geosci. Remote Sensing*, 27(1):36–45, January 1989.
- [29] M.A.M. Vissers and D.H. Hoekman. Efeda-spain: a ground truth data collection report. 1991.
- [30] J.R. Wang. The dielectric properties of soil-water mixtures at microwave frequencies. *Radio Sci.*, (15):977–985, 1980.

## Appendix A

# Soil moisture measurements

### A.1 1994 Soil moisture measurements

EMISAR flight Barley field	23/6/94 Track A	50 m between points Track B Peas/rape	Track Wheat	Dir.	Track Rape
0	24.4	38.3	33.7	N	32.3
50	39.1	34.2	32.9	N	30.5
100	19.4	19.5	26.8	N	28.7
150	28.9	39.1	29	N	35.5
200	34.3	38.5	33.3	N	32.6
250	34.2	33.7	28.4	N	20.3
300	15.7	31.1	27.4	N	19.8
350	29.5	23.4	32.8	S	28.8
400	33.8	23.5	26.2	S	29.9
450	32.8	25.7	rape?	S	34.8
500	13.6	37.4	rape?	S	36.7
550	34.3	25.4	rape?	S	32.2
600	30	22.3	rape?	S	38
650	21.5	32.1	rape?	S	36.2
700	32.2	30.6	rape?		
750	13.9	32.3			
800	32.6	26.9			
850	16.8	27.6			
900	34.3	28.2			
950	24.2	30.8			
1000	24.8	29.3			
1050	21	29.1			
1100	22.2	37.6			
1150	27	30.9			
1200	31.3	36.3			
1250	31.3	30.7			
1300	32.5	26.5			
1350	20.8	35.1			
1400	38.7	32.5			
1450	19.6	40.4			

Table A.1: TDR volumetric soil moisture content measurements performed on June 23, 1994

### A.2 1995 Soil moisture measurements

May 3, 1995						
Distance from edge	Track A		Track B		Track C	
	45degs	22.5degs	45degs	22.5degs	45degs	22.5degs
0	31.7	29.9	42.6	35.6	27.4	22.2
20	23.3	17.2	32.6	14.2	35.5	22.7
40	30.4	26	27.5	22.4	32.6	21.6
60	21.7	16.2	36.4	30.7	33.7	32.4
80	22.4	26.7	26.7	14.1	35.8	27.9
100	29.8	25.4	27.3	16.1	32.9	22.2
120	21.1	8.4	32.3	27.1	34.8	23.4
140	33.9	24.9	30.8	28.8	31.3	26.8
160	27.2	28	31.5	19.1	32	25.7
180	29.7	2.9	28	18.9	33.4	23.7
200	25.7	13.2	31.2	21.4	32	22
220	25.2	7.8	29.6	17.5	28.8	25.3
240	18.1	21.5	15.9	12.2	31.8	28.7
260	25.4	20.1	24.8	20.5	33.4	30.2
280	25.7	20.4	21.9	18.6	31	27.7
300	26.8	19	33.4	17.4	27.6	25.1
320	27.6	22	29	21.9	28.9	24.1
340	26.3	9.3	28.6	14.7	28.7	24.4
360	13.2	20.7	30.2	23.8	35	32
380	21.4	7.6	33.2	17.7	36.6	33.1
400	30.3	11.6	26.8	12.3	43.6	42
420	18	21.4	26.6	16.9	37.9	35.5
440	32.4	19.8	31.7	20.7	39.6	36.7
460	31.3	14.5	40.4	30.1	38.6	32
480	24.2	16.7	21.6	22.9	34.1	30.5
500	25	21.9	34	21.5	29.8	16.7
520	23.2	16.5	33.6	18.6	33.3	24.1
540	27.2	24.4	35.1	35.6	36	29
560	28	20.9	35.5	16.6	29.1	35
580	30.1	28.9	28.2	14.5	32.7	24
600	26.1	16.3	25.8	13.4	30.1	28.3
620	36.2	32.1	21	16.1	39.7	37.4
640	32.5	26.7	21.3	14.3	38	40.3
660	42	39.7	35.1	21.1	40.3	34
680	44	22.8	30.5	14.9		
700	43.6	42.4	25.8	11.8		
720	32.9	25	31.7	15.6		
740	37.4	33.5	28.9	14.9		
760	29.1	24				
780	31.7	19.3				

Table A.2: TDR volumetric soil moisture content measurements performed on May 3, 1995, Tracks A, B and C

May 3, 1995						
Distance from edge	Track D		Track E		Track F	
	45degs	22.5degs	45degs	22.5degs	45degs	22.5degs
0	29.8	24.2	23.8	20.3	30	31.8
20	34.4	33.5	22.4	16.7	26.5	14.1
40	29.2	28	26	11.7	28.7	11.3
60	33.2	29.2	23.8	14.1	30	18.1
70	30	25.6	22	11.3	25.7	17.5
80	29.1	25.6	27.9	26.6	22.2	21.5
100	31.2	27.5	26.5	22.6	34.7	23.8
120	35.2	32.7	22	21.6	28	18.3
140	29	23.3	24	19.7	28.7	20.6
160	25.9	18.7	22.8	9.6	33.5	22.5
180	28	25	28.2	12.2	29	8.9
200	17.8	17.4	27.6	21.5	31.4	25.8
220	25.5	15.4	20.8	20.2	33.8	25.4
240	29.4	25.9	23.7	16.5	34	15.1
260	27	22.2	24.7	12.6	33.1	22.5
280	26.6	18.6	21.8	16.2	34.5	30.9
300	25.3	21.1	28.4	23.5	37	32.9
320	25.9	19.3	29.3	17.2	27.3	12.2
340	17.9	22.2	29.8	24	24.1	30.6
360	27.8	20.7	32.2	11.6	26.7	19.9
380	27.9	24.2				
400	32.1	30				
420	32.8	30.9				
440	34.5	32.1				
460	29.1	33.4				
480	37.1	35				
500	33.9	31.2				
520	33.9	28.1				
540	29.4	23.5				
560	26.8	19.7				
580	27.1	20.5				
600	28.2	22.8				
620	28	15.3				
640	27.6	8.9				
660	28.5	17.4				
680	30	14.6				
700						

Table A.3: TDR volumetric soil moisture content measurements performed on May 3, 1995, Tracks D, E and F

distance from edge (m)	FIRST DAY: 5/7/95				SECOND DAY: 6/7/95			
	Track A moisture %		Track B moisture %		Track A moisture %		Track B moisture %	
	(20 degs)	(45 degs)	(20 degs)	(45 degs)	(20 degs)	(45 degs)	(20 degs)	(45 degs)
0	15.2	1.3	27.7	32.2	7.7	20.6	19.7	11.8
20	21.8	11.6	22.4	24.3	16.1	15.7	22.1	23
40	22.2	18.1	25.7	15.9	12.8	21.3	16.3	24.8
60	21.6	28.4	29.8	22	17.4	29.6	19.7	26.2
80	16.4	6.9	27.2	30.9	16.4	22	19	20
100	28.8	25.2	25.5	29.1	18	27	15	22.3
120	26.7	28.2	24.1	28.7	17.3	22.2	19	24
140	25.6	26.2	26.4	24.3	20.1	22	11.6	23.3
160	21.2	21	19.6	24.7	14.2	15.4	12.4	20.3
180	20.7	29.7	29	31.5	16.8	19.6	16	22.7
200	17.4	17.5	27.7	28.5	11.7	11.6	6.6	21.5
220	19.4	15.4	17.2	18.1	20.3	9.4	13.3	23.4
240	18.9	23.3	28.8	32.4	19.4	26.8	14.5	13.2
260	15.5	19	26.9	30.5	13.5	23.7	14.9	27.2
280	22.2	20.5	20.4	26.9	22.1	17	18.4	25.8
300	20.7	6.3	25.7	30.9	11.5	28.1	18.3	24.8
320	15.3	6.7	25.7	33.6	6.9	9.9	14.5	22.4
340	16	27	20.4	27.2	12.9	23.3	19.6	9.9
360	8.6	19.8	27.8	31.5	17.4	28.1	16.8	21.9
380	14.5	12.9	22.2	28.8	16.7	10.5	12.9	26.1
400	23.2	26.6	28.2	27.4	19.1	17.2	17.7	25.4
420	20.9	25.5	23.7	23.7	18.7	22.5	14.1	27.8
440	27.8	26.1	23.8	30.3	17.9	19.7	19.7	27.6
460	26.4	22.7	23.9	26.4	14.7	5.9	11.6	29.7
480	23.2	14.6	23.7	29.9	21.1	27.2	21.2	28
500	23.1	28.6	19.3	29.8	16.3	23.8	22.8	28.3
520	23.9	21.1	29.2	25.9	17.5	31.8	22.4	23
540	18.5	13.7	24.5	27.2	16.9	15.8	10	21.6
560	19	21.9	26.9	29.6	16.1	18	12.8	22.9
580	9.8	15.2	26.3	27.2	14.9	20.8	16.2	23.6
600	23.1	15	17.9	19.7	10	20.9	9.3	16.4
620	13.2	16.1	26.3	30.7	15.6	17.9	10.4	14.2
640	23.8	14.9	23.2	26.7	21.8	14.4	8.1	16.5
660	16.9	26.6	18.6	25.8	17.8	20.9	13.2	16.9
680	20.8	17.9	26.1	27.9	10.6	24.3	12.6	23
700			25.9	34.5	17.8	17.9	10.6	22.9
720					8.2	14.5		

Table A.4: TDR volumetric soil moisture content measurements performed on July 5 and 6, 1995, Tracks A and B

Distance from edge (m)	FIRST DAY: 5/7/95				SECOND DAY: 6/7/95			
	Track C moisture %		Track D moisture %		Track C moisture %		Track D moisture %	
	(20 degs)	(45 degs)	(20 degs)	(45 degs)	(20 degs)	(45 degs)	(20 degs)	(45 degs)
0	28.8	18	18	28	17.7	20	8.8	24
20	24.8	30.8	15.9	25.3	18	25.2	5.7	16
40	14.8	25	20.1	29	19.8	15.1	13.7	24
60	12.8	27.2	22.2	27.3	22.6	30.3	15.5	23.5
80	11	28.4	26.7	29.5	16	25.4	12.5	22
100	24.3	28.8	23.7	29.3	17.7	22.4	18.2	21.3
120	28.9	26.9	27.3	29.6	11.5	26.5	17.2	27.2
140	24.4	27.5	27.5	29	16	27.6	10.9	22.3
160	17.5	10.1	26.8	31.3	17.1	28.6	11	24.7
180	5.8	25.6	28.2	28.5	15.6	27.2	15.6	24.9
200	23.6	20.8	28.5	30.5	19.2	28.2	13.3	16.5
220	22.7	29.8	23.6	24.1	10	18	18.7	27.2
240	16.1	26.1	25.2	29.1	19.4	17.3	16.8	28.3
260	25.6	29.7	22.8	31.2	15	27.7	20.1	24.8
280	21.9	28.1	23	27.4	16.4	16.6	14.5	22.7
300	9.9	15.6	21.1	14.3	10.7	23.2	11.6	22.7
320	18.6	27.3	23.6	28.9	14.4	26.5	15.3	22.7
340	18.8	27.7	22.4	28.1	16.6	22.5	18.1	25.9
360	24.6	16.3	22.7	18.8	13	26.4	15.3	25.9
380	24.1	29	19.3	25.4	10.7	13.4	12.6	23.6
400	19.1	27.1	19.1	25.8	16.4	25.4	14.5	21.5
420	21.1	29.1	19.3	25.2	6.3	11.8	16.2	22.7
440	7.6	27.8	21.9	22	16.1	25.4	4.5	24.7
460	8.5	20.8	21	22.9	20.8	28.7	8.8	13.8
480	12	4.2	22.5	30.7	16.8	25.2	18.5	24.6
500	21.2	9.6	25.6	26.3	15.2	23.3	18	22.1
520	16	23.9	20.4	28.1	18.4	17.1	14.2	25.2
540	22.1	24.8	21.1	20.7	15.3	25.7	19.3	21.6
560	22.9	28.1	25.6	17.4	16.6	28.1	15.6	24.4
580	13	26.3	15.6	18.1	18.4	13.9	12.1	21.3
600	16.9	22.6	24.7	28.8	14.7	26.4	17.1	26.4
620	11.7	30.9	22.9	32.4	22.5	10.9	21.2	24.5
640	8.1	21	24	29.2	14.5	25.7	10.4	20.8
660	24.9	28.8	25.8	33.6	19.8	28.9	18.5	16.7
680	22.9	29			18.7	29		
700								

Table A.5: TDR volumetric soil moisture content measurements performed on July 5 and 6, 1995, Tracks C and D

Distance from edge (m)	FIRST DAY: 5/7/95				SECOND DAY: 6/7/95			
	Track F moisture %		Track E moisture %		Track F moisture %		Track E moisture %	
	(20 degs)	(45 degs)	(20 degs)	(45 degs)	(20 degs)	(45 degs)	(20 degs)	(45 degs)
0	21	16.3	15.4	18.1	8.5	32.7	12.9	22
20	8.4	11.2	14.5	25.4	10.2	25.4	24.2	30.7
40	21.6	17.7	27.6	28.7	14.7	12	16.2	23.6
60	13.2	26.6	26.3	33.9	17.7	27	24	29.1
80	13.4	30	22.9	30.1	19.2	27.1	15.6	23.4
100	12.5	26.3	28	31.4	18.6	27.9	13.3	21.7
120	22.7	25.4	23.4	32	14.6	26.5	25	30.8
140	14.8	16.6	23.6	29.7	-	-	13.1	19.1
160	-	-	25.3	29.4	-	-	19	-
180	-	-	20.2	24.8	-	-	14.4	26
200	-	-	22.7	27.7	-	-	18	27.8
220	26.9	27.5	21.2	22.3	17.8	27.5	18.8	22.9
240	17	24.8	27.2	34.4	13.8	21.5	15	20.9
260	18	23.7	21.9	25.1	17.4	24	19.9	28.8
280	8.5	21.5	29.4	32.1	14.9	21.9	17.9	30.2
300	22.8	26.6	15.7	22.4	21	25	18.8	29.7
320	17.9	25.4	27.3	31.7	12.9	24	15.1	26.3
340	10.4	28.4	17.3	18	20.2	26.6	21.7	26.7
360	10.2	27.3	25.2	31.6	14.7	27.9	11	23.2
380	11.7	19.4	21.5	29.9	26.8	23	21.8	24.4
400	10.3	23.7	-	-	15	17.3	-	-
420	25.5	28.6	-	-	15.1	19.7	-	-
440	-	-	-	-	17.6	21.5	-	-
460	-	-	-	-	17.6	18.8	-	-

Table A.6: TDR volumetric soil moisture content measurements performed on July 5 and 6, 1995, Tracks E and F

## Appendix B

# Forest Floor Cross-Sections

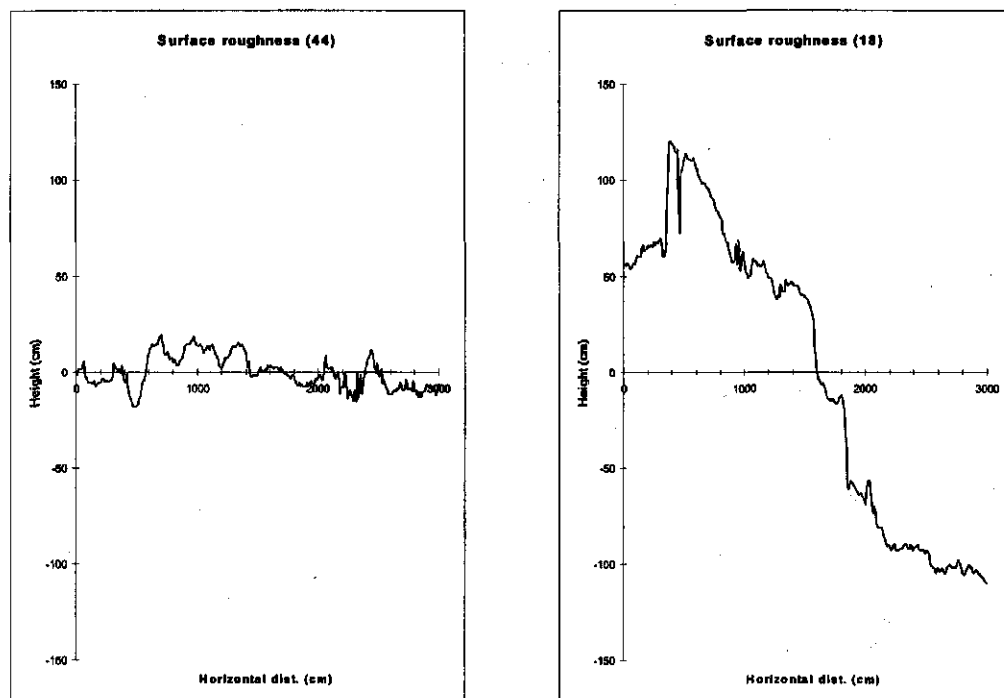


Figure B.1: Long transect height profile measurements for stands 18 and 44

bearing dist (cm)	220° relative depth (cm)	300° relative depth (cm)	bearing dist (cm)	220° relative depth (cm)	300° relative depth (cm)
0	124	141	500	112	136
10	125	141	510	111	137
20	127	138	520	111	137
30	130	137	530	111	136
40	132	135	540	110	126
50	132	139	550	111	131
60	133	138	560	111	131
70	131	136	570	110	130
80	131	137	580	112	132
90	131	137	590	113	133
100	132	121	600	112	133
110	131	112	610	113	132
120	132	109	620	113	135
130	132	108	630	111	136
140	131	105	640	112	138
150	125	107	650	113	139
160	127	112	660	111	138
170	128	120	670	111	138
180	127	132	680	112	138
190	126	132	690	113	137
200	127	137	700	111	137
210	126	140	710	109	137
220	126	140	720	110	137
230	125	140	730	111	138
240	124	140	740	110	139
250	124	139	750	111	140
260	121	138	760	111	140
270	123	139	770	110	140
280	123	137	780	110	141
290	122	134	790	109	138
300	122	136	800	108	139
310	119	139	810	108	137
320	117	138	820	106	135
330	117	139	830	105	134
340	116	138	840	106	133
350	116	138	850	106	133
360	115	139	860	104	131
370	116	139	870	105	130
380	116	139	880	104	129
390	115	139	890	101	128
400	117	139	900	97	129
410	117	140	910	95	131
420	119	140	920	95	132
430	119	140	930	95	134
440	118	138	940	99	134
450	116	135	950	100	134
460	117	136	960	102	136
470	113	127	970	98	137
480	111	138	980	97	136
490	114	135	990	96	135
			1000	94	135

Table B.2: Cross section height measurements for stand 8B



Bearing dist (cm)	220° relative depth (cm)	300° relative depth (cm)	Bearing dist (cm)	220° relative depth (cm)	300° relative depth (cm)
0	189	168	500	213	162
10	188	167	510	213	162
20	189	167	520	213	162
30	190	166	530	213	159
40	190	167	540	212	158
50	189	167	550	212	160
60	187	167	560	212	162
70	184	168	570	212	160
80	186	166	580	210	161
90	191	165	590	210	160
100	190	166	600	211	160
110	184	165	610	212	160
120	196	165	620	212	161
130	198	166	630	211	162
140	199	167	640	214	161
150	200	169	650	210	161
160	199	168	660	205	163
170	200	167	670	212	164
180	201	168	680	212	164
190	202	167	690	215	165
200	200	166	700	215	166
210	194	168	710	217	168
220	193	168	720	217	168
230	197	166	730	218	168
240	199	165	740	219	166
250	202	169	750	217	166
260	203	165	760	217	165
270	204	165	770	219	166
280	206	166	780	220	166
290	208	167	790	217	166
300	207	167	800	215	168
310	208	167	810	213	169
320	208	163	820	212	167
330	208	161	830	211	167
340	209	164	840	211	167
350	208	162	850	215	166
360	210	161	860	218	166
370	210	158	870	217	165
380	210	162	880	216	166
390	211	166	890	215	166
400	209	166	900	213	165
410	209	168	910	209	165
420	209	164	920	207	163
430	211	163	930	208	161
440	210	163	940	204	158
450	209	165	950	204	155
460	209	166	960	205	154
470	211	164	970	209	152
480	212	165	980	212	149
490	213	165	990	216	146
			1000	218	142

Table B.1: Cross section height measurements for stand 8A

bearing dist (cm)	40° relative depth (cm)	120° relative depth (cm)	bearing dist (cm)	40° relative depth (cm)	120° relative depth (cm)
0	127	111	500	130	97
10	127	111	510	131	98
20	127	108	520	129	101
30	126	110	530	127	101
40	129	106	540	128	104
50	127	93	550	126	105
60	126	87	560	126	105
70	126	83	570	124	105
80	128	82	580	124	104
90	127	80	590	118	103
100	125	78	600	116	102
110	127	81	610	116	102
120	127	84	620	115	103
130	126	91	630	120	104
140	128	96	640	121	110
150	127	99	650	121	112
160	130	102	660	115	111
170	128	103	670	115	114
180	128	103	680	115	111
190	130	105	690	118	113
200	131	109	700	120	114
210	126	109	710	118	114
220	126	109	720	117	114
230	128	108	730	120	112
240	129	109	740	120	110
250	127	109	750	121	104
260	126	109	760	117	107
270	132	111	770	117	109
280	129	110	780	119	112
290	129	102	790	121	112
300	130	80	800	123	110
310	131	79	810	124	110
320	130	81	820	123	109
330	128	87	830	120	106
340	126	95	840	120	108
350	127	93	850	120	107
360	128	91	860	113	104
370	127	88	870	105	98
380	131	85	880	102	99
390	130	82	890	102	98
400	129	81	900	105	95
410	128	77	910	109	95
420	128	80	920	115	90
430	128	89	930	114	95
440	129	93	940	112	94
450	128	95	950	114	96
460	124	93	960	113	101
470	114	94	970	115	107
480	114	90	980	113	110
490	128	96	990	112	113
			1000	118	111

Table B.3: Cross section height measurements for stand 17

bearing dist (cm)	170° relative depth (cm)	250° relative depth (cm)	bearing dist (cm)	170° relative depth (cm)	250° relative depth (cm)
0	121	86	500	130	97
10	121	85	510	131	98
20	121	86	520	129	101
30	121	86	530	127	101
40	121	87	540	128	104
50	122	88	550	126	105
60	122	90	560	126	105
70	120	93	570	124	105
80	118	78	580	124	104
90	123	105	590	118	103
100	124	83	600	116	102
110	125	80	610	116	102
120	125	79	620	115	103
130	124	78	630	120	104
140	125	76	640	121	110
150	124	75	650	121	112
160	125	74	660	115	111
170	123	76	670	115	114
180	119	82	680	115	111
190	120	86	690	118	113
200	120	97	700	120	114
210	117	115	710	118	114
220	117	123	720	117	114
230	117	124	730	120	112
240	116	124	740	120	110
250	117	117	750	121	104
260	115	118	760	117	107
270	111	118	770	117	109
280	109	123	780	119	112
290	105	122	790	121	112
300	104	121	800	123	110
310	103	122	810	124	110
320	105	122	820	123	109
330	108	119	830	120	106
340	110	120	840	120	108
350	110	119	850	120	107
360	113	119	860	113	104
370	113	121	870	105	98
380	113	120	880	102	99
390	114	121	890	102	98
400	106	120	900	105	95
410	107	122	910	109	95
420	110	120	920	115	90
430	110	121	930	114	95
440	109	119	940	112	94
450	109	120	950	114	96
460	107	117	960	113	101
470	107	120	970	115	107
480	106	119	980	113	110
490	106	120	990	112	113
			1000	115	111

Table B.4: Cross section height measurements for stand 18A

bearing dist (cm)	250° relative depth (cm)	325° relative depth (cm)	bearing dist (cm)	250° relative depth (cm)	325° relative depth (cm)
0	202	161	500	200	167
10	200	160	510	203	162
20	200	159	520	203	158
30	203	161	530	207	158
40	204	168	540	210	156
50	202	168	550	210	153
60	203	166	560	205	154
70	202	167	570	201	149
80	202	169	580	201	149
90	201	171	590	205	151
100	204	183	600	206	155
110	206	184	610	199	157
120	203	180	620	203	162
130	201	181	630	204	169
140	201	182	640	206	171
150	200	181	650	207	173
160	201	181	660	207	176
170	199	179	670	200	176
180	201	177	680	195	179
190	201	179	690	203	180
200	201	178	700	208	181
210	199	177	710	208	179
220	201	177	720	210	179
230	202	175	730	204	180
240	204	171	740	209	182
250	203	166	750	206	183
260	202	174	760	204	183
270	198	168	770	204	183
280	196	172	780	206	185
290	197	176	790	208	181
300	196	180	800	210	186
310	197	183	810	208	186
320	196	182	820	206	186
330	195	183	830	204	186
340	196	183	840	203	187
350	195	183	850	202	188
360	195	182	860	203	189
370	198	179	870	200	182
380	200	177	880	199	186
390	204	175	890	199	187
400	204	179	900	204	187
410	206	180	910	204	187
420	205	176	920	205	190
430	204	179	930	207	188
440	202	182	940	206	186
450	198	184	950	203	184
460	195	181	960	206	184
470	188	179	970	206	184
480	188	175	980	205	183
490	207	173	990	206	184
			1000	203	183

Table B.5: Cross section height measurements for stand 18B

bearing dist (cm)	70° relative depth (cm)	160° relative depth (cm)	bearing dist (cm)	70° relative depth (cm)	160° relative depth (cm)
0	199	183	500	214	198
10	200	191	510	219	198
20	202	192	520	218	199
30	205	193	530	215	198
40	206	194	540	216	201
50	210	179	550	212	201
60	212	188	560	211	203
70	212	189	570	211	205
80	214	194	580	213	205
90	213	188	590	212	205
100	210	194	600	213	207
110	209	194	610	212	207
120	207	195	620	210	207
130	206	194	630	208	206
140	208	196	640	207	204
150	205	196	650	201	202
160	205	198	660	202	198
170	204	199	670	201	191
180	203	200	680	201	192
190	203	199	690	200	192
200	201	200	700	200	195
210	203	199	710	200	197
220	201	202	720	195	206
230	199	203	730	201	210
240	206	204	740	205	216
250	209	207	750	205	217
260	210	209	760	204	219
270	208	210	770	203	220
280	214	209	780	205	217
290	216	210	790	206	218
300	217	208	800	206	216
310	220	198	810	205	215
320	222	204	820	203	218
330	223	204	830	199	217
340	223	201	840	198	210
350	222	198	850	197	213
360	223	200	860	198	215
370	223	200	870	196	213
380	225	200	880	201	212
390	224	197	890	204	213
400	227	198	900	204	213
410	226	198	910	207	213
420	225	195	920	213	214
430	224	196	930	214	216
440	224	194	940	214	215
450	218	196	950	212	213
460	217	196	960	213	214
470	219	194	970	207	215
480	217	197	980	204	213
490	215	199	990	203	208
			1000	206	209

Table B.6: Cross section height measurements for stand 20.1 (clear cut)

bearing dist (cm)	290° relative depth (cm)	40° relative depth (cm)	bearing dist (cm)	290° relative depth (cm)	40° relative depth (cm)
0	153	155	500	125	89
10	151	153	510	120	91
20	151	154	520	117	99
30	151	154	530	115	98
40	150	142	540	112	95
50	149	143	550	107	93
60	148	143	560	105	92
70	150	137	570	101	93
80	150	143	580	100	97
90	152	138	590	99	100
100	152	144	600	103	109
110	148	144	610	103	115
120	146	144	620	105	118
130	146	143	630	108	120
140	145	143	640	109	125
150	146	141	650	110	131
160	147	143	660	108	127
170	147	144	670	106	128
180	143	138	680	109	116
190	139	142	690	111	113
200	139	141	700	115	110
210	138	143	710	117	105
220	147	143	720	119	101
230	149	143	730	120	102
240	149	143	740	121	100
250	143	119	750	120	97
260	143	125	760	124	94
270	145	137	770	124	86
280	144	137	780	124	90
290	142	135	790	125	120
300	138	134	800	125	125
310	136	134	810	123	124
320	136	132	820	118	126
330	141	122	830	117	125
340	142	122	840	117	123
350	142	116	850	115	123
360	140	116	860	113	122
370	136	117	870	113	122
380	140	115	880	114	120
390	140	108	890	115	119
400	131	105	900	117	119
410	137	102	910	120	117
420	135	98	920	120	118
430	133	98	930	121	116
440	131	94	940	121	117
450	134	93	950	121	123
460	134	89	960	121	125
470	132	91	970	122	125
480	129	90	980	122	130
490	126	90	990	120	84
			1000	105	76

Table B.7: Cross section height measurements for stand 021

bearing dist (cm)	350° relative depth (cm)	280° relative depth (cm)	bearing dist (cm)	350° relative depth (cm)	280° relative depth (cm)
0	170	165	500	117	180
10	170	163	510	116	176
20	170	164	520	116	175
30	147	167	530	114	177
40	147	167	540	111	186
50	146	164	550	111	187
60	147	163	560	109	186
70	146	162	570	114	184
80	145	163	580	110	182
90	145	184	590	109	181
100	142	165	600	101	181
110	142	165	610	103	182
120	143	165	620	102	180
130	144	165	630	100	184
140	144	164	640	101	186
150	143	165	650	105	186
160	142	165	660	108	188
170	142	158	670	110	188
180	142	168	680	111	188
190	142	189	690	110	188
200	139	166	700	109	186
210	139	168	710	110	187
220	139	170	720	110	186
230	137	170	730	108	180
240	136	166	740	108	180
250	130	170	750	105	178
260	126	172	760	105	182
270	127	162	770	104	182
280	135	162	780	104	183
290	135	164	790	105	180
300	132	166	800	107	177
310	130	173	810	102	174
320	130	174	820	107	174
330	128	175	830	106	178
340	127	177	840	106	177
350	126	173	850	103	176
360	122	178	860	100	174
370	119	179	870	105	172
380	120	178	880	103	170
390	121	178	890	101	171
400	122	168	900	100	169
410	121	167	910	90	170
420	122	180	920	88	165
430	123	180	930	93	162
440	120	181	940	97	164
450	121	180	950	99	166
460	120	179	960	100	166
470	119	179	970	103	166
480	119	182	980	104	165
490	117	171	990	105	163
			1000	105	162

Table B.8: Cross section height measurements for stand 042

bearing dist (cm)	300° relative depth (cm)	220° relative depth (cm)	bearing dist (cm)	300° relative depth (cm)	220° relative depth (cm)
0	145	176	500	162	160
10	145	178	510	160	162
20	145	176	520	158	162
30	145	178	530	155	160
40	146	176	540	152	160
50	147	175	550	153	158
60	148	176	560	153	153
70	148	172	570	152	159
80	149	171	580	155	159
90	150	168	590	156	160
100	152	165	600	160	160
110	153	161	610	163	159
120	154	156	620	165	160
130	155	151	630	167	160
140	156	149	640	169	162
150	156	146	650	170	163
160	156	142	660	172	160
170	155	141	670	173	167
180	155	139	680	171	168
190	157	143	690	169	168
200	159	149	700	172	169
210	159	149	710	170	172
220	161	145	720	170	175
230	161	150	730	168	176
240	161	149	740	168	176
250	162	142	750	167	177
260	161	140	760	165	177
270	160	140	770	160	176
280	160	141	780	162	177
290	160	145	790	160	177
300	158	150	800	160	175
310	158	160	810	159	175
320	155	156	820	157	174
330	156	162	830	144	170
340	154	164	840	153	171
350	153	164	850	153	171
360	154	163	860	152	170
370	153	165	870	150	171
380	153	166	880	148	171
390	154	162	890	147	172
400	156	163	900	145	174
410	156	166	910	141	174
420	156	162	920	141	173
430	157	165	930	134	176
440	156	165	940	136	175
450	158	165	950	136	170
460	159	163	960	140	176
470	158	161	970	142	166
480	160	162	980	141	174
490	160	161	990	140	177
			1000	141	175

Table B.9: Cross section height measurements for stand 044

bearing dist (cm)	70° relative depth (cm)	160° relative depth (cm)	bearing dist (cm)	70° relative depth (cm)	160° relative depth (cm)
0	126	175	500	132	218
10	130	177	510	131	220
20	133	179	520	130	220
30	134	182	530	123	221
40	136	182	540	124	220
50	139	181	550	126	223
60	142	180	560	126	224
70	141	181	570	128	225
80	137	181	580	136	226
90	134	182	590	139	227
100	131	184	600	140	227
110	130	187	610	140	228
120	128	187	620	135	230
130	125	187	630	133	231
140	125	189	640	130	232
150	124	189	650	128	233
160	126	189	660	122	234
170	128	190	670	125	234
180	135	191	680	128	235
190	140	193	690	128	236
200	140	195	700	126	237
210	140	195	710	125	237
220	135	197	720	134	238
230	132	200	730	138	239
240	128	199	740	139	240
250	127	198	750	139	241
260	124	199	760	133	242
270	127	200	770	132	243
280	128	200	780	130	244
290	125	199	790	129	244
300	126	201	800	123	245
310	131	202	810	123	245
320	140	203	820	125	245
330	140	206	830	127	247
340	141	207	840	128	250
350	140	210	850	132	250
360	132	209	860	136	249
370	130	212	870	137	249
380	130	214	880	139	250
390	128	217	890	137	251
400	125	220	900	131	252
410	123	216	910	132	253
420	123	215	920	127	253
430	128	214	930	125	254
440	129	216	940	125	255
450	135	217	950	126	255
460	137	218	960	124	256
470	137	217	970	127	257
480	137	219	980	131	259
490	135	219	990	138	260
			1000	143	261

Table B.10: Cross section height measurements for stand 46.1



## **Appendix C**

### **Forest stand parameters**

Stand No.	Area (ha)	Age (yrs)	%Pine	%Spruce	%Other
033.2	2.1	57	20	80	0
034	5.5	70	80	20	0
034.1	2.7	59	0	90	10
035	1.3	70	40	60	0
036	12.9	88	100	0	0
036.1	5.9	30	100	0	0
037	16.1	26	70	20	10
038	7.2	14	100	0	0
039	7.3	4	60	40	0
039.1	0.8	-	-	-	-
040	3.8	61	50	40	10
041	2.9	40	100	0	0
042	4.9	28	100	0	0
043	4.8	27	70	10	20
044	7.4	66	70	30	0
044.1	3.2	5	0	100	0
045	3.3	39	0	90	10
045.1	1.3	61	10	50	40
046	2.9	37	90	10	0
046.1	6.1	37	0	100	0
047	5.4	70	30	60	10

Table C.1: Swedish Forestry Service data for the stands in the Siggefora area. Ages are in 1994.